Scalable Synthesis of Pre-Intercalated Manganese(III/IV) Oxide Nanostructures for Supercapacitor Electrodes: Electrochemical Comparison of Birnessite and Cryptomelane Products

Daniel R. Jones,*[a] Haytham E. M. Hussein,[b] Eleri A. Worsley,[a] Sajad Kiani,[a] Kittiwat Kamlungsua,[c] Thomas M. Fone,[a] Christopher O. Phillips,[a] and Davide Deganello[a]

Manganese(III/IV) oxide is a promising pseudocapacitive material for supercapacitor electrodes due to favorable attributes such as its chemical resilience, high earth abundance and low specific cost. Herein, the morphological, compositional and electrochemical characteristics of co-precipitated manganese(III/IV) oxide products, each described by the general formula $Na_xK_yMnO_z$, are investigated to establish how these properties are influenced by synthesis conditions. $Na_xK_yMnO_z$ growths in low-temperature ($<100\,°C$) basic and acidic environments are shown to promote the formation of turbostratic birnessite and cryptomelane phases, respectively, with the latter polymorph containing a relatively low concentration of interstitial Na^+ and K^+ cations. It is demonstrated that K^+ pre-insertion during synthesis yields lower initial charge-transfer resistances than equivalent Na^+ intercalation, and that this parameter correlates strongly with storage performance. Accordingly, Na-mediated storage initially delivers inferior specific capacitances and Coulombic efficiencies than K-based mechanisms, but K^+ intercalation/deintercalation causes faster capacitance decay during prolonged galvanostatic cycling. Furthermore, whilst crystallographic phase is shown to have a weaker effect on $Na_xK_yMnO_z$ storage properties than the choice of intercalating guest cations, cryptomelane electrodes are more susceptible to cycling-induced capacitance and efficiency losses than their birnessite counterparts. In combination, these insights provide an instructive foundation for the optimization of $Na_xK_yMnO_z$ in high-power storage applications.

Introduction

If inherently intermittent renewable energy technologies are to offer a practical alternative to conventional heat engines, it is critically important that efficient, cost-effective and sustainable energy storage solutions are developed to decouple supply and demand profiles. A promising strategy is to pair the competitive energy densities of batteries with the superior cycling lifetimes and power densities of supercapacitors,[1] employing an appropriate maximum power point tracking (MPPT) system to optimize energy exchange between these complementary devices.[2] Mixed-valence manganese(III/IV) oxides (MnO_z, where z ranges between 1.5 and 2.0) have emerged as foremost candidates for the electroactive material in supercapacitor cathodes due to their low toxicity, minimal cost,[3] ready availability (manganese appears at an average concentration of ca. 1,000 ppm in the Earth's crust[4]), wide electrochemical stability window (ca. 1.0 V in aqueous electrolytes[5]), and high maximum theoretical specific capacitance (ca. 1,370 $F\,g^{-1}$, based on the reduction of Mn^{4+} ions by a single electron[6]). Charge storage in MnO_z is predominantly mediated by the pseudocapacitive intercalation of cations from the surrounding electrolyte in each discharge phase, followed by deintercalation of these guest ions during charging; in the case of a monovalent cation (A^+), this cyclical process is described by the reversible reaction scheme expressed in Equation 1,[7]

$$MnO_z + A^+ + e^- \leftrightarrow MnO_zA \tag{1}$$

where Mn^{4+} ions in MnO_z are reduced to the $3+$ oxidation state by participating electrons (e^-). Accordingly, effective storage performance is contingent on the accessibility of Mn^{4+} sites, and hence it is essential that cations can travel unimpeded throughout a charge-discharge cycle.

Of the various crystallographic phases of MnO_z, cryptomelane (α-MnO_z) and birnessite (δ-MnO_z) polymorphs are deemed two of the most promising candidates for storage applications because they possess characteristically wide channels for

[a] Dr. D. R. Jones, E. A. Worsley, Dr. S. Kiani, T. M. Fone, Dr. C. O. Phillips, Prof. D. Deganello
Faculty of Science and Engineering
Swansea University
Swansea, SA1 8EN (UK)
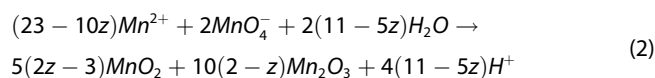E-mail: d.r.jones@swansea.ac.uk
[b] Dr. H. E. M. Hussein
School of Natural and Computing Sciences
University of Aberdeen
Aberdeen, AB24 3UE (UK)
E-mail: h.hussein@abdn.ac.uk
[c] Dr. K. Kamlungsua
Enserv Power Co. Ltd., Enserv Innovation Centre
Bangkok, 10800 (Thailand)
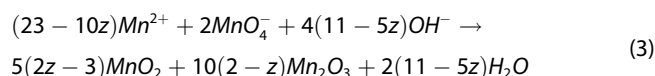E-mail: kittiwat@enserv.co.th

ChemElectroChem

Research Article
doi.org/10.1002/celc.202300210

**Chemistry
Europe**
European Chemical
Societies Publishing

intercalation/deintercalation:[8,9] α-MnO$_z$ consists of ca. 4.6 Å-diameter one-dimensional tunnels enclosed between corner-sharing MnO$_6$ octahedra, whereas δ-MnO$_z$ comprises two-dimensional layers of MnO$_6$ octahedra separated by ca. 7.0 Å. In both cases, these spacious passages result in a theoretical specific integral capacitance, C_{int}, that compares favorably with the corresponding storage capabilities of alternative phases such as tetragonal β-MnO$_z$ and orthorhombic γ-MnO$_z$.[8] In order to quantitatively assess α-MnO$_z$ and δ-MnO$_z$ products reported in the literature, it is instructive to collate the associated C_{int} values estimated from galvanostatic discharge measurements at a consistent current density. For this purpose, Figure 1 relates the discharge capacitances of selected α-MnO$_z$ and δ-MnO$_z$ materials to the temperature at which they were formulated, T_{synth}. The plotted data correspond to a gravimetric current density of 10 A per gram of electroactive material, with synthesis methods including the reduction of MnO$_4^-$ anions,[10–18] the oxidation of Mn^{2+} cations,[19–21] and the co-precipitation of Mn(II) and Mn(VII) sources[22–28] in acidic or alkaline conditions according to the multi-step reactions described in Equation 2,

$$(23-10z)Mn^{2+} + 2MnO_4^- + 2(11-5z)H_2O \rightarrow$$
$$5(2z-3)MnO_2 + 10(2-z)Mn_2O_3 + 4(11-5z)H^+ \qquad (2)$$

and Equation 3,

$$(23-10z)Mn^{2+} + 2MnO_4^- + 4(11-5z)OH^- \rightarrow$$
$$5(2z-3)MnO_2 + 10(2-z)Mn_2O_3 + 2(11-5z)H_2O \qquad (3)$$

respectively.[22] Whilst most of the products represented in Figure 1 were prepared at temperatures in excess of 100 °C, the weak correlation between C_{int} and T_{synth} suggests that lower synthesis temperatures do not necessarily yield inferior storage performance. Moreover, reducing T_{synth} below the boiling point of water provides a way to minimize the energy cost of MnO$_z$ production whilst maximizing the scalability of the process.
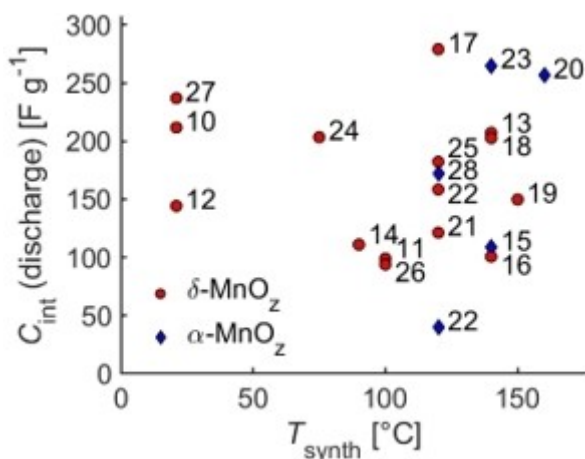
Figure 1. Literature values[10–28] of the specific integral capacitance, C_{int}, estimated from galvanostatic discharge measurements at 10 A g^{-1} and normalized with respect to the mass of electroactive material, plotted as a function of synthesis temperature, T_{synth}, for birnessite (δ-MnO$_z$) and cryptomelane (α-MnO$_z$) products.

Alongside specific capacitance and the electrochemical stability window, another key property of any supercapacitor electrode is its capacitance retention over many thousands of galvanostatic charge-discharge cycles.[29] In the case of aqueous MnO$_z$ systems, capacitance fading is known to depend strongly on the ability of the material to recover from repeated sequences of contraction and expansion caused by electrostatic attractions between the negatively charged MnO$_6$ octahedra and the guest cations.[30,31] Alternatively, deterioration may result from the disproportionation of Mn^{3+} ions at sufficiently low potentials (typically less than ca. −0.1 V vs Ag|AgCl (3 M KCl)),[30] generating Mn(II) products that can subsequently dissolve in the aqueous electrolyte.[29,30] Mass loss through dissolution can be circumvented by selecting an appropriate voltage range for electrochemical testing, whilst pre-inserting cations into the bulk material during synthesis also suppresses Mn reduction and enhances structural stability by reducing the propensity of the MnO$_6$ octahedra to shift during cycling.[15,29,32–36] In addition, the form of the MnO$_z$ polymorph is known to play a critical role in capacitance decay; for instance, it has been shown that Jahn-Teller distortions of MnO$_6$ octahedra cause less disruption to the two-dimensional channels of δ-MnO$_z$ than the corresponding ion pathways of α-MnO$_z$.[37]

Although numerous investigations into the electrochemical behaviors of MnO$_z$ materials have addressed how storage performance depends on factors such as crystallographic phase[22,37–44] and the nature of intercalating cations,[11,14,25,31,45–54] the effects of guest cation type and MnO$_z$ structure are rarely explored simultaneously within a single self-consistent study. Furthermore, researchers have hitherto adhered to a convention of measuring storage parameters as functions of current density and potential scan rate at just one stage during testing, either with the electrode in its as-prepared state or after a designated number of activation cycles.[11] The variation of capacitance retention is typically evaluated at a single value of current density during prolonged galvanostatic cycling, but, to the present authors' knowledge, all previous works have neglected to consider the evolution of established pre-cycling relationships over the full range of current density and potential scan rate values. For example, Xiong et al.[31] employed X-ray diffractometry (XRD) to link cyclical changes in the interlayer spacing of δ-MnO$_z$ to the intercalation/deintercalation of various cations, and it was shown that reducing the amplitude of lattice contraction and expansion yielded an improvement in capacitance retention over 5,000 galvanostatic cycles at 5 A g^{-1}. In turn, the authors reasoned that in comparison to mechanisms involving Li$^+$, Na$^+$ or Mg^{2+} ions, the relatively low structural deformation caused by K$^+$ exchanges translated to superior cycling stability. However, prior to the cycling procedure, it was demonstrated that storage performance depended strongly on current density, with K-mediated storage delivering lower capacitance than corresponding Li$^+$, Na$^+$ and Mg^{2+} processes below ca. 1 A g^{-1}, despite offering the highest capacitance when current density exceeded ca. 2 A g^{-1}. As the effects of current density on capacitance and Coulombic efficiency were not explored in the aftermath of prolonged

ChemElectroChem

Research Article
doi.org/10.1002/celc.202300210

**Chemistry
Europe**
European Chemical
Societies Publishing

cycling, it is unclear whether the inferred relationships between guest ion type and capacitance fading at 5 A g^{-1} are applicable over the whole current density range.

The present treatment avoids the identified shortcomings of previous research by quantifying the storage properties of α-MnO$_z$ and δ-MnO$_z$ electrodes, each described by the general formula Na$_x$K$_y$MnO$_z$, across various operating regimes, both before and after subjecting the electrodes to many galvanostatic charge-discharge cycles. In contrast to existing methodologies, this rigorous and systematic approach enables the short- and long-term effects of cation intercalation/deintercalation mechanisms to be elucidated in enhanced detail over the full duration of electrochemical testing. Alongside these electrode measurements, a variety of other characterization techniques were implemented to explore the influence of synthesis pH and guest cation type on the morphology, composition and crystallography of the resulting Na$_x$K$_y$MnO$_z$ product. By examining these relationships in greater detail than existing investigations, the present research serves as an instructive resource for the optimization of mixed-valence

Na$_x$K$_y$MnO$_z$, providing a scalable basis to develop efficient, stable and charge-dense pseudocapacitive cathodes for use in high-power storage applications.

Results and Discussion

Phase Identification

Through the co-precipitation of Mn^{2+} and MnO$_4^-$ ions, Na$_x$K$_y$MnO$_z$ samples were prepared under either basic (B) or acidic (A) conditions; for concision, materials produced in the presence of Na$_2$SO$_{4(aq)}$ are henceforth assigned the prefix "Na", whilst the prefix "K" is used to reference products obtained when K$_2$SO$_{4(aq)}$ was instead used as a synthesis precursor. X-ray diffraction (XRD) measurements acquired from the four Na$_x$K$_y$MnO$_z$ products (Figure 2) indicate that the choice of cation in the sulfate salt had a seemingly negligible effect on crystallographic structure, although the predominant polymorph was altered by changing the pH of the synthesis solution: the XRD
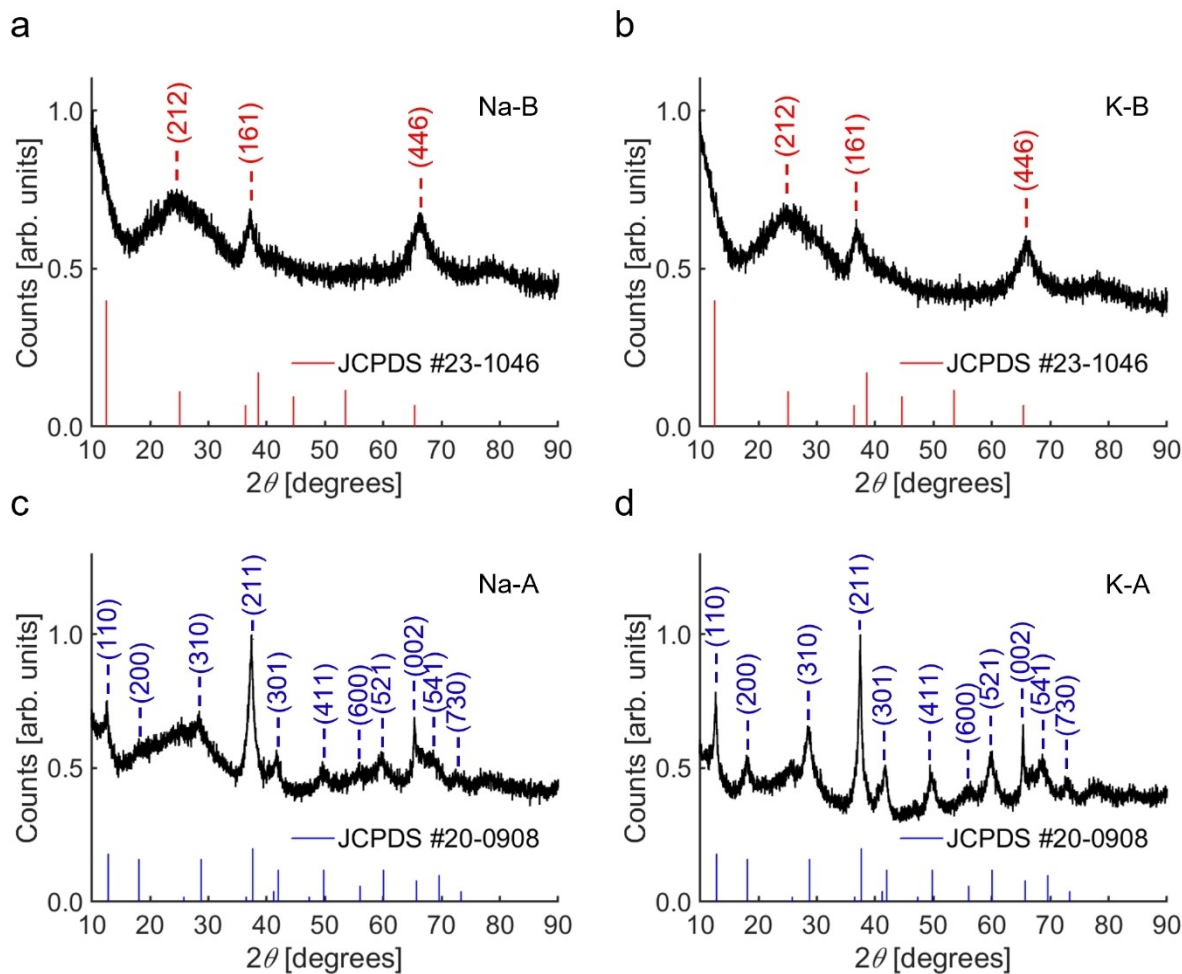
Figure 2. Transmission-mode powder X-ray diffractograms acquired from samples of Na-B (a), K-B (b), Na-A (c) and K-A (d); crystallographic peaks associated with turbostratic birnessite δ-MnO$_z$ and cryptomelane α-MnO$_z$ are indexed to reference patterns provided by JCPDS cards 23-1046 and 20-0908, respectively.

ChemElectroChem

Research Article
doi.org/10.1002/celc.202300210

**Chemistry
Europe**
European Chemical
Societies Publishing

patterns of Na-B and K-B (Figure 2a and b, respectively) are consistent with the lamellar structure of birnessite MnO_z (δ-MnO_z), as indexed by JCPDS card 23-1046,[55] whereas the diffractograms of samples Na-A and K-A (Figure 2c and d) accord with tetragonal cryptomelane MnO_z (α-MnO_z), corresponding to JCPDS card 20-0908.[56] A notable feature of the birnessite systems is the apparent absence of the (002) peak, which characteristically appears at a 2θ value of ca. 12.5°; this omission suggests that Na-B and K-B did not adopt the archetypal form of pristine δ-MnO_z. Indeed, similar suppression of the (002) peak has been witnessed in the X-ray diffractograms of other Na- and K-intercalated δ-MnO_z products,[14,25,57,58] and the phenomenon may be attributed to poor alignment between lattice planes due to turbostratic stacking of the δ-MnO_z nanosheets.[59] Conversely, the Na-A and K-A diffractograms both contain sharp peaks matching the full reference pattern of α-MnO_z, which shows that as well as promoting formation of the cryptomelane phase, acidic conditions also enhanced lattice ordering.

The relationship between $Na_xK_yMnO_z$ crystallography and synthesis pH has been considered in previous research,[22,38,60] wherein it has been demonstrated that the principal polymorph depends on the relative concentrations of hydroxonium and alkali metal cations: cryptomelane structures preferentially form when there is a sufficient abundance of hydroxonium ions to competitively intercalate into the one-dimensional channels, whilst lower hydroxonium availability causes MnO_6 octahedra to instead assemble as two-dimensional layers. As the relatively narrow tunnel configuration of α-MnO_z renders it less vulnerable than δ-MnO_z to infiltration by electrolyte species, the formation of well-ordered crystallites in δ-MnO_z is more strongly inhibited by pre-insertion processes. Consequently, literature comparisons between the X-ray diffractograms of α-MnO_z and turbostratic δ-MnO_z[8,22,38,61,62] typically reveal that a much higher degree of crystallinity exists in the cryptomelane case.

By examining each sample using a combination of field-emission scanning electron microscopy (SEM), transmission electron microscopy (TEM) and scanning transmission electron microscopy (STEM), the relationship between lattice structure and synthesis pH was further explored (Figure 3). Images of the samples prepared under basic conditions, Na-B (Figure 3a–c) and K-B (Figure 3d–f), show that they consisted of microscale particles with nanoscopic surface features, which are representative of agglomerated δ-MnO_z nanoflakes[8] exemplified elsewhere in the literature.[13,25,61] In TEM images of Na-B and K-B (Figure 3c and f, respectively), no lattice planes were discernible amongst the turbostratic δ-MnO_z matrix; this finding is consistent with the low signal-to-noise ratio of the corresponding X-ray diffractograms (Figure 2a and b, respectively) and the absence of (002) peaks in these measurements. By contrast, SEM and TEM images acquired from the products of acidic synthesis conditions, Na-A (Figure 3g–i) and K-A (Figure 3j–l), indicate that they possessed a high degree of crystallinity, evidenced by an abundance of nanorods consisting of well-defined lattice planes and atomic columns (Figure 3i and l, and Figure S1 of the Supporting Information). Lattice d-spacing measurements obtained from the high-magnification TEM

images of Na-A (Figure 3i, and Figure S1a and b) and K-A (Figure 3l, and Figure S1c and d) may be indexed to characteristic peaks in the XRD patterns of Na-A (Figure 2c) and K-A (Figure 2d), with examples of (110), (200) and (310) plane arrangements identified in the images. Nevertheless, it should be noted that both Na-A and K-A also contained high quantities of seemingly amorphous particles, akin to the microstructures of Na-B and K-B. It is thus apparent that whilst the acidic growth environments of Na-A and K-A encouraged nanorod formation, this process was accompanied by alternative co-precipitation mechanisms that culminated in a more disordered product.

Composition Analysis

The chemical compositions of the four $Na_xK_yMnO_z$ products were investigated by X-ray photoelectron spectroscopy (XPS); Mn 2p, O 1s, C 1s, Na 1s, and K 2p spectra were acquired from four separate locations on the surface of each pelletized sample. XPS data obtained from one region of the Na-A pellet are provided in Figure 4, whilst the Supporting Information displays corresponding measurements from Na-B (Figure S2), K-B (Figure S3), and K-A (Figure S4). To illustrate the magnitude of composition variations across each pellet surface, the Supporting Information also includes overlaid presentations of the survey spectra (Figure S5) and the Mn 2p (Figure S6), O 1s (Figure S7), C 1s and K 2p (Figure S8), and Na 1s (Figure S9) measurements from the four sample locations, normalizing the measured count rate with respect to the relevant Mn $2p_{3/2}$ peak maximum in each case; in all of these comparisons, it is clear that the shape and intensity of the core peaks varied little between the scanned areas. By deconvolving the core spectra into constituent components associated with distinct electronic environments, it is possible to estimate the relative proportions of chemical species; the mean and standard deviation of atomic ratios from the four pellet locations were calculated in order to evaluate the significance of chemical differences between samples.

In general, MnO_6 octahedra generated by the co-precipitation of Mn^{2+} and MnO_4^- ions are composed of Mn(III) and Mn(IV) oxidation states; consequently, the Mn 2p spectra of Na-B (Figure S2a), K-B (Figure S3a), Na-A (Figure 4a) and K-A (Figure S4a) can be resolved into two pairs of doublets, with the $2p_{3/2}$ components of the Mn(III) and Mn(IV) species centred at characteristic binding energies of ca. 640.6–641.0 eV and ca. 642.1–642.3 eV, respectively.[14,15,63–68] From the relative areas of these doublets it is evident that Na-A and K-A comprised a higher proportion of Mn^{3+} environments than Na-B and K-B, implying that basic synthesis conditions suppressed the reduction of Mn^{4+} ions; this deduction concurs with previous research on co-precipitated cryptomelane and turbostratic birnessite MnO_z, which has demonstrated that α-MnO_z inherently possesses a lower average oxidation state than δ-MnO_z.[62,69] By comparing the relative areas of the Mn(III) and Mn(IV) components from each set of four sample locations, Mn^{3+}/Mn^{4+} ratios of 0.07 ± 0.03 and 0.42 ± 0.05 are obtained for Na-B and K-B, respectively, which are considerably lower
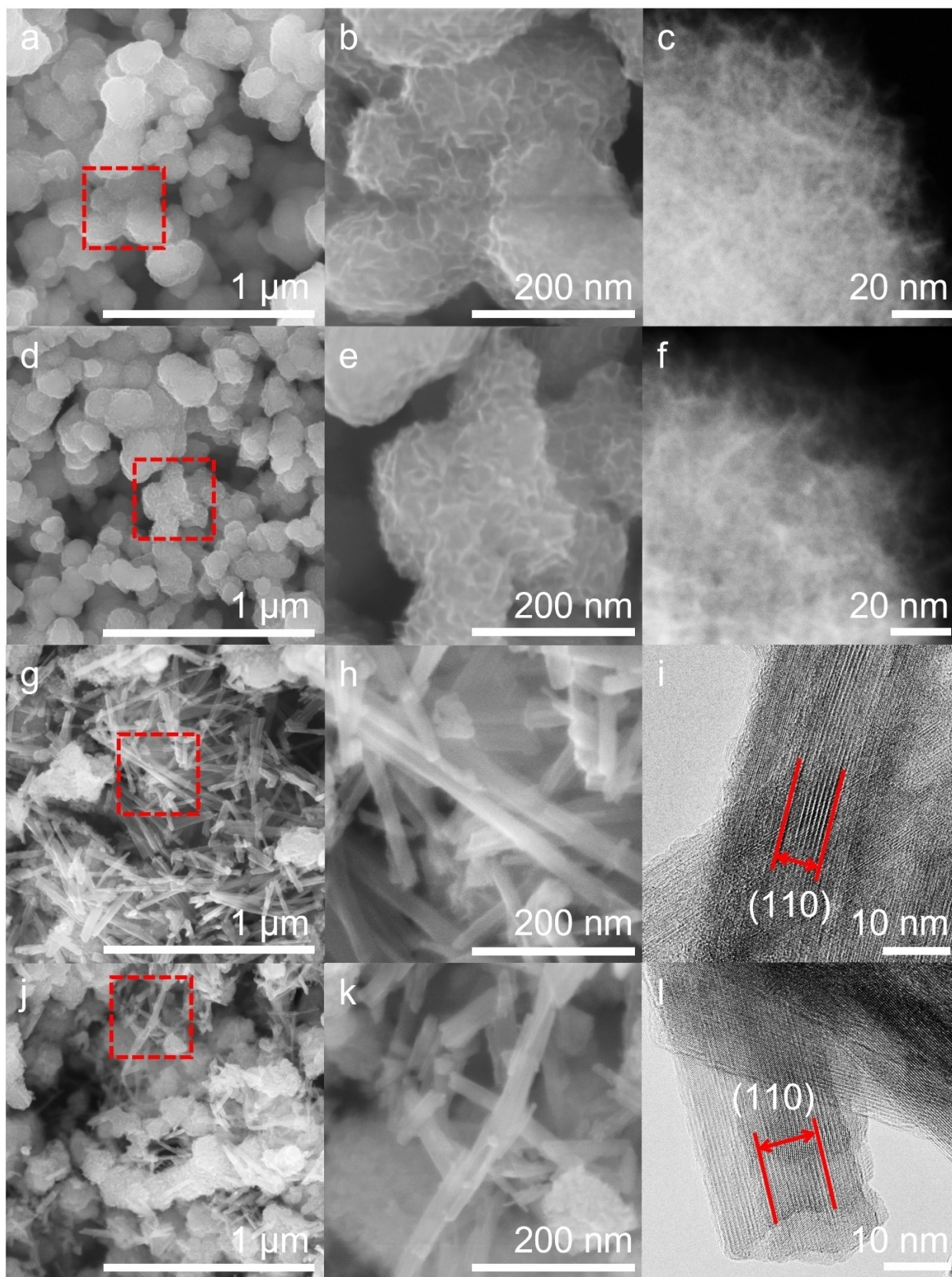
Figure 3. Field-emission SEM (a, b, d, e, g, h, j and k) and TEM/STEM (c, f, i and l) images acquired from Na-B (a–c), K-B (d–f), Na-A (g–i) and K-A (j–l); STEM images corresponding to Na-B (c) and K-B (f) suggest that these samples consisted of randomly oriented agglomerates of birnessite (δ-MnO_2) nanoflakes, whereas distinctive collections of well-aligned crystallographic lattice planes corresponding to the cryptomelane (α-MnO_2) phase are discernible within the TEM images of Na-A (i, and Figure S1a and b of the Supporting Information) and K-A (l, and Figure S1c and d of the Supporting Information), as indicated in the images. In the lowest magnification SEM images (a, d, g and j), the regions surveyed at higher magnification (b, e, h and k) are marked by dashed red boxes.
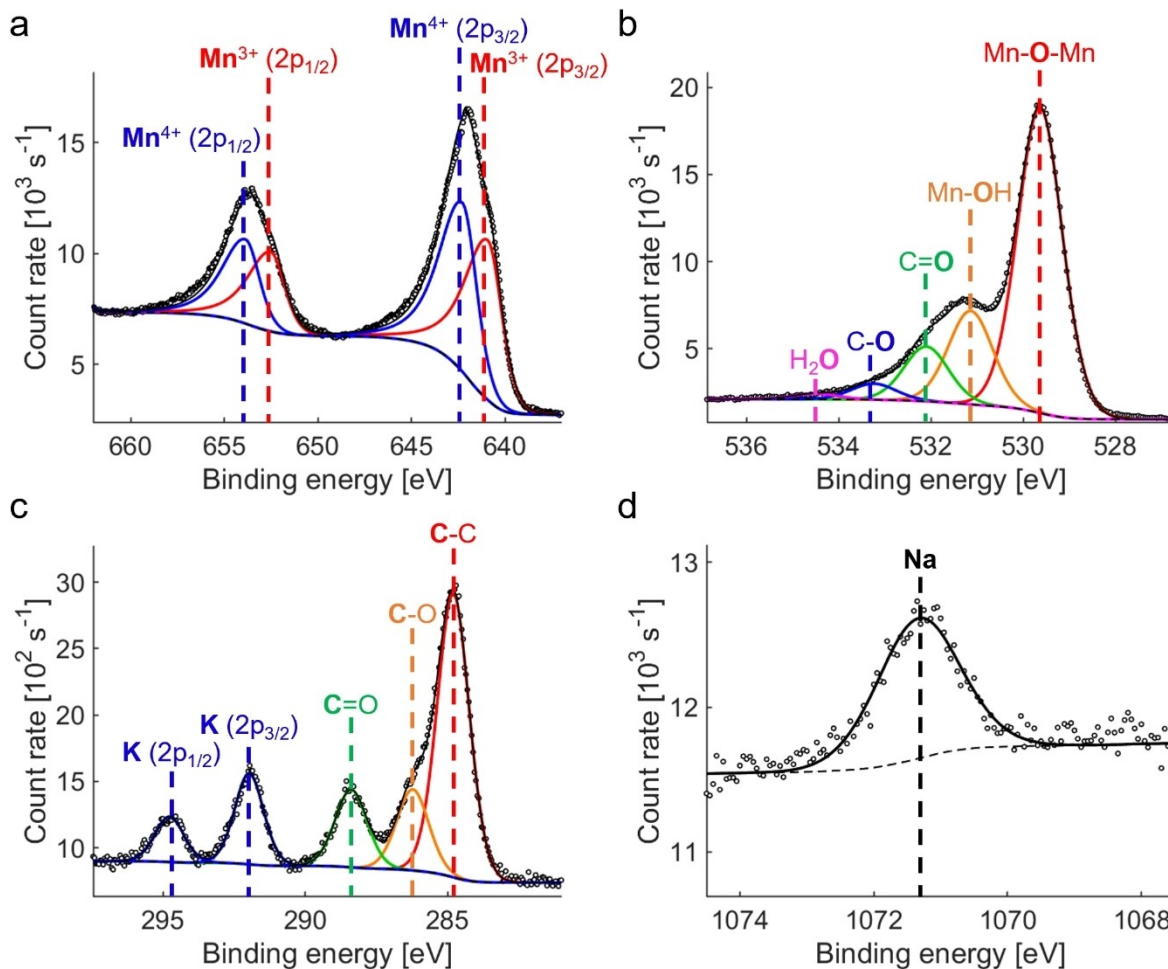
Figure 4. X-ray photoelectron measurements from Na-A, including the Mn 2p (a), O 1s (b), K 2p and C1s (c), and Na 1s (d) core peaks. Deconvolution of these spectra was achieved by fitting Gaussian-Lorentzian (O 1s, K 2p, C 1s and Na 1s) or asymmetric Lorentzian (Mn 2p) functions to the data following subtraction of a Shirley-type background function. For clarity, components associated with separate electronic environments are represented by different colors, whilst the $2p_{3/2}$ and $2p_{1/2}$ contributions of a given 2p doublet are assigned the same color. The proposed species responsible for the plotted spectral components are annotated accordingly, and the peak position of each component is indicated by a vertical dashed line.

than corresponding values of 0.97 ± 0.05 and 0.88 ± 0.05 yielded, respectively, by the Mn 2p spectra of Na-A and K-A.

The Na/Mn and K/Mn atomic ratios, respectively denoted x and y in the general formula $Na_xK_yMnO_z$, may be similarly estimated from the XPS measurements. K 2p spectra recorded from Na-B (Figure S2c), K-B (Figure S3c), Na-A (Figure 4c) and K-A (Figure S4c) all exhibit a doublet that is well-represented by a single electronic environment, located at binding energies in the vicinity of C 1s components from the adventitious organic surface layer.[70] Similarly, the Na 1s spectra of Na-B (Figure S2d) and Na-A (Figure 4d) consist of one symmetric peak, indicative of a single Na species. From the enclosed areas of the Na 1s and Mn 2p spectra, a mean Na/Mn atomic ratio of 0.30 ± 0.03 is obtained for Na-B, which compares with a corresponding value of 0.044 ± 0.006 from the Na-A data. No Na 1s signal was observed in the case of K-B (Figure S3d) or K-A (Figure S4d), as no Na-containing precursors were involved during formulation of these materials. It is also apparent that basic synthesis conditions facilitated intercalation of K$^+$ ions, as K-B possessed

a mean K/Mn atomic ratio of 0.39 ± 0.02, which is three times greater than a corresponding estimate of 0.130 ± 0.001 yielded by the K 2p and Mn 2p doublets of K-A. As anticipated from the low concentration of K-based precursors employed in their syntheses, Na-B and Na-A comprised far lower quantities of pre-inserted K$^+$ ions: the relative magnitudes of associated K 2p and Mn 2p spectra are consistent with mean K/Mn atomic ratios of 0.040 ± 0.002 and 0.043 ± 0.001 for Na-B and Na-A, respectively. A qualitative rationale for the differing levels of pre-intercalation within the acidic and basic samples may be developed by recalling the crystallographic structures of the α-MnO$_z$ and δ-MnO$_z$ polymorphs: the planar configuration of MnO$_6$ octahedra in δ-MnO$_z$ provides wide interlayer passages for ionic transport, in contrast to the comparatively narrow one-dimensional channels of α-MnO$_z$.[8]

To determine the mean O/Mn atomic ratio within each sample, denoted z in the general formula $Na_xK_yMnO_z$, it is necessary to analyse the contributions of Mn-containing species to corresponding O 1s spectra. Due to the high surface-

ChemElectroChem

Research Article
doi.org/10.1002/celc.202300210

Chemistry Europe
European Chemical
Societies Publishing

sensitivity of the XPS technique, each O 1s spectrum contains components associated with C−O and C=O environments from the thin adventitious organic layer that enveloped the particles, in addition to interstitial water.[71–73] These species were accompanied by O^{2-} anions situated in the bulk MnO_z lattice and Mn-bound hydroxide groups with characteristic O 1s peaks centred at binding energies of ca. 529.6–530.0 eV and ca. 531.1–531.4 eV, respectively,[64,65,72,73] which must be summed to determine the overall quantity of O that was affiliated with the octahedral MnO_6 units. By comparing these combined contributions to the total atomic percentages of Mn, respective z estimates of 1.92 ± 0.02 and 1.91 ± 0.04 are computed from the O 1s spectra of Na-B (Figure S2b) and K-B (Figure S2c), which far exceed corresponding values of 1.604 ± 0.008 and 1.639 ± 0.008 yielded by the O 1s spectra of Na-A (Figure 4b) and K-A (Figure S4b), respectively.

A summary of key results from the XRD and XPS characterizations is provided in Table 1, which collates the identified crystallographic phases of Na-B, K-B, Na-A and K-A alongside the estimated mean atomic ratios Na/Mn (x), K/Mn (y) and O/Mn (z). Also included in Table 1 are the Brunauer-Emmett-Teller (BET) specific surface areas of the four products estimated via the Supporting Information (Figure S10), which depicts the measured Type IV isotherms[74,75] of Na-B (Figure S10a), K-B (Figure S10c), Na-A (Figure S10e) and K-A (Figure S10g) in conjunction with BET plots (Figure S10b, d, f and h, respectively) constructed from the nitrogen adsorption curves. As observed in previous $Na_xK_yMnO_z$ research,[14,38,65,68] each pair of adsorption and desorption isotherms is separated by a H3 hysteresis loop,[74,75] which is indicative of condensation at mesopores present within the material. The BET specific surface areas of Na-A and K-A were found to be an order of magnitude greater than those of their basic counterparts, reflecting the nanoscopic dimensions of the α-MnO_z crystallites. The high abundance of mesoporous adsorption sites in Na-A and K-A is also evident from their hysteresis loops, which are appreciably more pronounced than the corresponding hysteresis behaviors of Na-B and K-B.

Electrochemical Performance Testing

To assess the electrochemical stability of the $Na_xK_yMnO_z$ products, and to explore the nature of charge storage mechanisms in the presence of alkali metal cations, $Na_xK_yMnO_z$ electrodes were subjected to cyclic voltammetry (CV) sweeps at potential scan rates, ν, in the ranges 10–100 mV s^{-1} (Figure 5)

and 100–$1,000$ mV s^{-1} (Figure S11 of the Supporting Information). Prior to galvanostatic charge-discharge (GCD) cycling, the as-prepared electrodes of Na-B (Figure 5a and Figure S11a), K-B (Figure 5c and Figure S11c), Na-A (Figure 5e and Figure S11e) and K-A (Figure 5g and Figure S11g) all exhibited near-rectangular relationships between potential, E, and current density, J, at scan rates ranging from 10 mV s^{-1} to 100 mV s^{-1} (Figure 5a, c, e and g). However, after performing 2,000 successive galvanostatic cycles at 28.6 A g^{-1} between 0.0 V and 1.0 V vs Ag|AgCl (3 M KCl), the corresponding cyclic voltammograms (Figure 5b, d, f and h) diverged significantly from the rectangular form of an ideal supercapacitor,[76] especially at the upper limit of the scanned potential window. A notable aspect of these post-cycling CV measurements is the emergence of redox peaks at potentials close to 0.5 V vs Ag|AgCl (3 M KCl), which are especially evident in the cases of Na-B (Figure 5b) and Na-A (Figure 5f); similar redox features observed in the voltammograms of other $Na_xK_yMnO_z$ electrodes have been assigned to the Mn^{4+}/Mn^{3+} redox couple, accompanied by reversible alkali metal cation intercalation/deintercalation.[15,31,34,44,77–79] Increasing the potential scan rate to 100–$1,000$ mV s^{-1} caused the J vs ν relationships of Na-B (Figure S11a and b), K-B (Figure S11c and d), Na-A (Figure S11e and f) and K-A (Figure S11g and h) to deviate from the linear J vs ν trend witnessed during slower CV scans, both in the as-prepared state (Figure S11a, c, e and g) and after prolonged galvanostatic cycling (Figure S11b, d, f and h).

Further analysis of the pre- and post-cycling voltammograms was achieved via application of the Dunn formula (Equation 4),[80]

$$J = k_{surf}\nu + k_{diff}\nu^{1/2} \qquad (4)$$

where the term containing the constant coefficient k_{surf} represents the linear J vs ν trend yielded by fast pseudocapacitive processes at the electrode surface, and the term possessing a square-root dependence on ν, with a constant coefficient k_{diff}, corresponds to diffusion-controlled ion exchange mechanisms. In conjunction with Equation 4, it is possible to assess the relative contributions of surface- and diffusion-mediated storage interactions by plotting the quotient $|J|/\nu^{1/2}$ as a function of $\nu^{1/2}$ (Figure S12 of the Supporting Information), as the coefficients k_{surf} and k_{diff} are given, respectively, by the gradient and y-intercept of the relationship between these quantities. Applying this approach to pre- and post-cycling J measurements from the CV data of Na-B (Figure S12a), K-B (Figure S12b), Na-A (Figure S12c) and K-A (Figure S12d) at 0.5 V vs Ag|AgCl

Table 1. Compiled mean atomic ratio estimates determined from the deconvolved XPS spectra of Na-B (Figure S2), K-B (Figure S3), Na-A (Figure 4) and K-A (Figure S4), alongside the principal crystallographic phases identified from XRD measurements (Figure 2) and specific surface areas calculated through BET analysis of nitrogen adsorption isotherms (Figure S10).

$Na_xK_yMnO_z$ sample	Mean atomic ratios			Principal phase	BET specific surface area [m^2 g^{-1}]
	Na/Mn (x)	K/Mn (y)	O/Mn (z)		
Na-B	0.30 ± 0.03	0.040 ± 0.002	1.92 ± 0.02	Birnessite	21.4
K-B	0.000	0.39 ± 0.02	1.91 ± 0.04	Birnessite	29.0
Na-A	0.044 ± 0.006	0.043 ± 0.001	1.604 ± 0.008	Cryptomelane	181.0
K-A	0.000	0.130 ± 0.001	1.639 ± 0.008	Cryptomelane	151.0
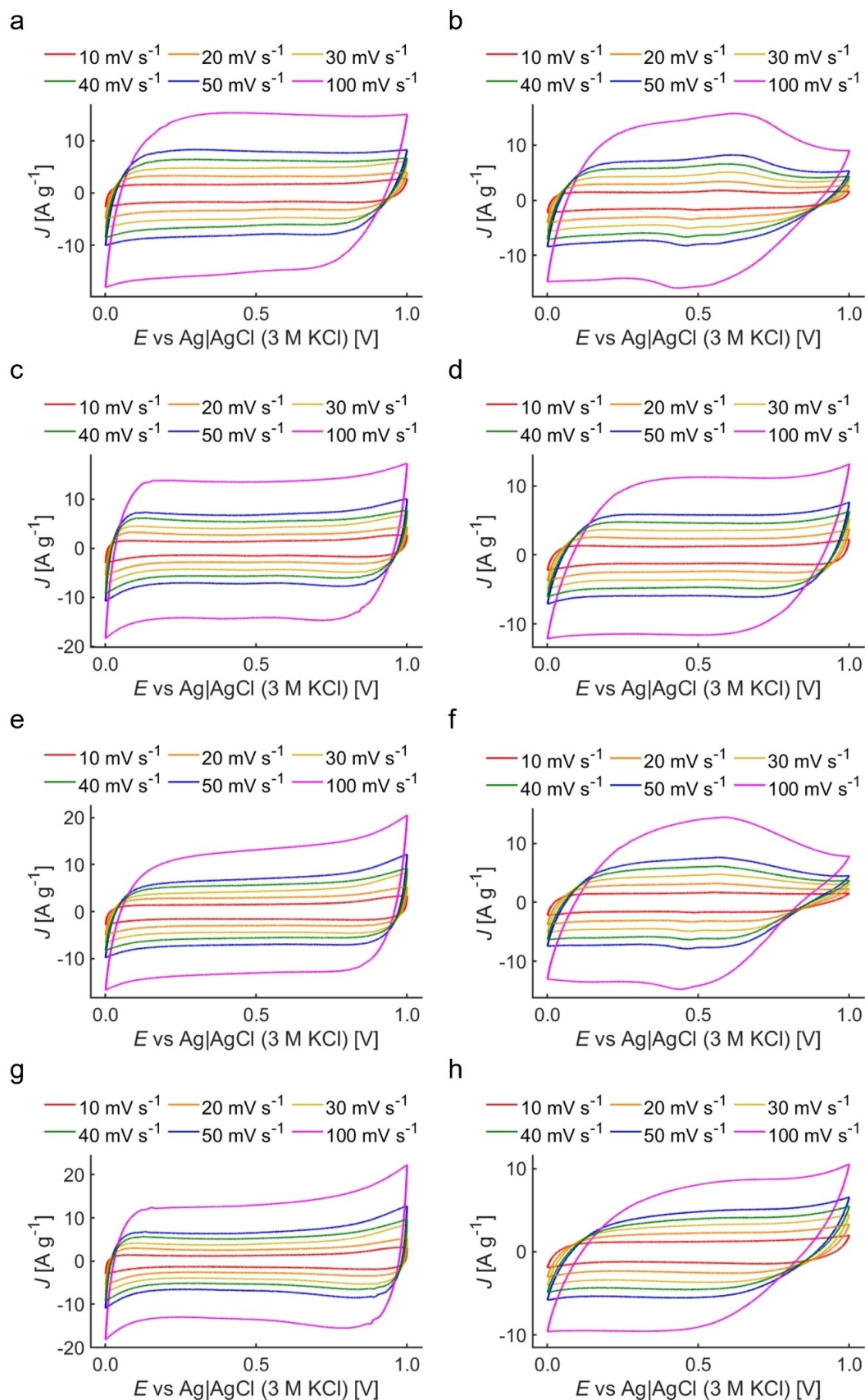
Figure 5. Cyclic voltammograms measured at potential scan rates, ν, between 10 mV s⁻¹ and 100 mV s⁻¹, both before (a, c, e and g) and after (b, d, f and h) subjecting the Na-B (a and b), K-B (c and d), Na-A (e and f) and K-A (g and h) electrodes to 2,000 GCD cycles at a current density of 28.6 A g⁻¹.

ChemElectroChem

Research Article
doi.org/10.1002/celc.202300210

**Chemistry
Europe**
European Chemical
Societies Publishing

(3 M KCl), it is clear that the displayed relationships adhere to the Dunn equation up to ν values of ca. 100 mV s^{-1}, whereupon they diverge from the predicted linearity between $|J|/\nu^{1/2}$ and $\nu^{1/2}$. Na-B and Na-A were most weakly affected by the cycling procedure, whilst more marked mechanistic changes in the K-based products, K-B and K-A, are evident from the greater discrepancies between their pre- and post-cycling $|J(0.5\ V)|/\nu^{1/2}$ vs $\nu^{1/2}$ trends.

Repeating Dunn's protocol over the entirety of the cyclic voltammogram at a given value of ν enables estimation of the surface-mediated storage contributions. As shown in the Supporting Information (Figure S13), these mechanisms accounted for most of the transferred power within the central plateau of CV measurements acquired at 50 mV s^{-1}, but diffusion-controlled processes delivered an increasing proportion of the total current density close to the extrema of the spanned potential range. In agreement with the $|J(0.5\ V)|/\nu^{1/2}$ vs $\nu^{1/2}$ relationships depicted in Figure S12, prolonged galvanostatic cycling had a seemingly weak effect on surface contributions in Na-B (Figure S13a and b) and Na-A (Figure S13e and f): integration of the pre-cycling surface current curves reveals that pseudocapacitive charge exchange delivered 88% (Figure S13a) and 83% (Figure S13e), respectively, of total current in these systems, compared with 91% (Figure S13b) and 86% (Figure S13f), respectively, in the post-cycling case. Conversely, pre-cycling surface contributions of 90% in both K-B (Figure S13c) and K-A (Figure S13g) decreased to post-cycling values of 87% (Figure S13d) and 79% (Figure S13h), respectively.
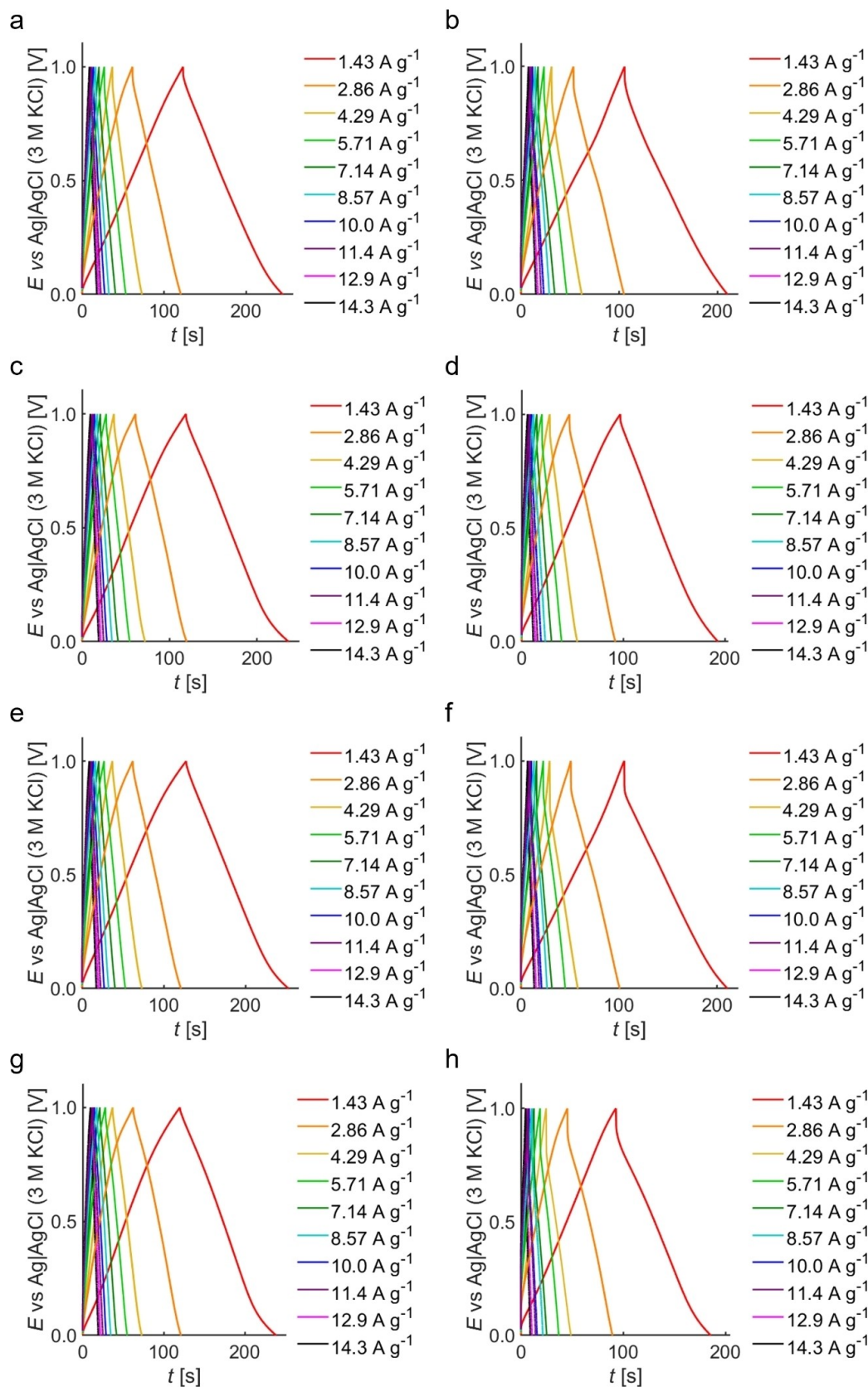
The specific integral capacitances, C_{int}, of the Na$_x$K$_y$MnO$_z$ electrodes were quantified for charging and discharging between 0.0 V and 1.0 V vs Ag|AgCl (3 M KCl) by considering GCD measurements acquired over the current density ranges 1.43–14.3 A g^{-1} (Figure 6) and 14.3–143 A g^{-1} (Figure S14 of the Supporting Information), both before (Figure 6a, c, e and g, and Figure S14a, c, e and g) and after (Figure 6b, d, f and h, and Figure S14b, d, f and h) conducting 2,000 galvanostatic cycles at 28.6 A g^{-1}. To map the evolution of GCD behaviors, the Supporting Information (Figure S15) also provides overlaid depictions of the 2,000 cycles performed by each system (Figure S15a, c, e and g), alongside the measured variations in discharge capacitance retention (Figure S15b, d, f and h). It was observed in all cases that the durations of the charge and discharge phases diminished gradually during prolonged cycling, equilibrating at a decreased value of C_{int} and increased equivalent series resistance (ESR); the latter property is directly proportional to the instantaneous potential change at a given charge-discharge transition,[76,81] and hence it is measurable at both the upper and lower threshold of the spanned potential window (0.0 V and 1.0 V). Of the four samples, Na-B (Figure S15a and b) experienced the lowest rate of capacitance decay, delivering a capacitance retention of 89% after 2,000 cycles. By comparison, K-B (Figure S15c and d) retained 75% of its initial discharge capacitance by the end of the cycling process, whilst the cryptomelane samples, Na-A (Figure S15e and f) and K-A (Figure S15g and h), exhibited markedly inferior retention values of 60% and 46%, respectively. It should be noted that since C_{int} effectively averages the capacitance of a given system

over the measured E range, its application as a storage metric should be restricted to cases where differential capacitance, which correlates with the instantaneous rate of potential variation, dE/dt, at a given location on the GCD curve, exhibits negligible potential-dependence.[76] In the present case, every dataset depicted in Figure 6 and Figure S14 is characterized by a strongly linear relationship between E and time t, indicating that differential capacitance indeed remained approximately constant for the duration of each GCD experiment.

By constructing linear fits over the charge and discharge regions of the GCD measurements, the variation of C_{int} was estimated as a function of J (Figure 7) for Na-B (Figure 7a and b), K-B (Figure 7 c and d), Na-A (Figure 7e and f) and K-A (Figure 7g and h), both before (Figure 7a, c, e and g) and after (Figure 7b, d, f and h) prolonged galvanostatic cycling. Additionally, the Coulombic efficiencies, η_Q, of the pre- and post-cycled systems were estimated at each J value (Figure S16 of the Supporting Information) by computing the ratio of the cumulative charge transferred to and from the electrodes during the relevant charge-discharge cycle. Even though the four Na$_x$K$_y$MnO$_z$ products comprised two different polymorphs and displayed varying levels of cation pre-insertion, the as-prepared electrodes delivered remarkably similar storage characteristics up to current densities on the order of 10 A g^{-1}; indeed, differences between C_{int} estimates associated with galvanostatic discharge at 10 A g^{-1} (Table 2) are of comparable magnitude to the corresponding experimental uncertainties. At higher current densities, pre-cycling pseudocapacitance was more significantly influenced by the intrinsic properties of guest cations, with K-B and K-A initially delivering greater values of C_{int} and η_Q at 100 A g^{-1} than the Na-based electrodes. However, K-B and K-A subsequently experienced a faster cycling-induced decline in storage performance than Na-B and Na-A, evidenced by the relatively large separations between their pre- and post-cycling the η_Q vs J trends. The post-cycling inferiority of the K-intercalated systems is most apparent from capacitance measurements acquired at high current density; for instance, the C_{int} values exhibited by K-B and K-A at 100 A g^{-1} (Table 2) are an order of magnitude lower than the corresponding estimates yielded by Na-B and Na-A. The comparatively pronounced destabilization caused by K$^+$ intercalation/deintercalation is reflective of the substantial discrepancies between the pre- and post-cycling $|J(0.5\ V)|/\nu^{1/2}$ vs $\nu^{1/2}$ behaviors of K-B (Figure S12b) and K-A (Figure S12d), which are much greater than corresponding differences between the $|J(0.5\ V)|/\nu^{1/2}$ vs $\nu^{1/2}$ relationships of Na-B (Figure S12a) and Na-A (Figure S12c).

Table 2. Pre- and post-cycling estimates of the specific integral capacitance, C_{int}, exhibited by the four Na$_x$K$_y$MnO$_z$ samples under discharge at current densities of 10 A g^{-1} and 100 A g^{-1}.

Na$_x$K$_y$MnO$_z$ sample	Pre-cycling C_{int} (discharge) [F g^{-1}]		Post-cycling C_{int} (discharge) [F g^{-1}]	
	10 A g^{-1}	100 A g^{-1}	10 A g^{-1}	100 A g^{-1}
Na-B	155 ± 6	70 ± 3	146 ± 5	50 ± 3
K-B	149 ± 6	96 ± 4	116 ± 5	4.6 ± 0.6
Na-A	141 ± 5	71 ± 3	138 ± 5	22.0 ± 1.3
K-A	146 ± 5	94 ± 4	112 ± 4	5.6 ± 0.6

ChemElectroChem

Research Article
doi.org/10.1002/celc.202300210

**Chemistry
Europe**
European Chemical
Societies Publishing

Figure 6. Pre- (a, c, e and g) and post-cycling (b, d, f and h) GCD behaviors of Na-B (a and b), K-B (c and d), Na-A (e and f) and K-A (g and h) measured at current densities between 1.43 A g^{-1} and 14.3 A g^{-1}.
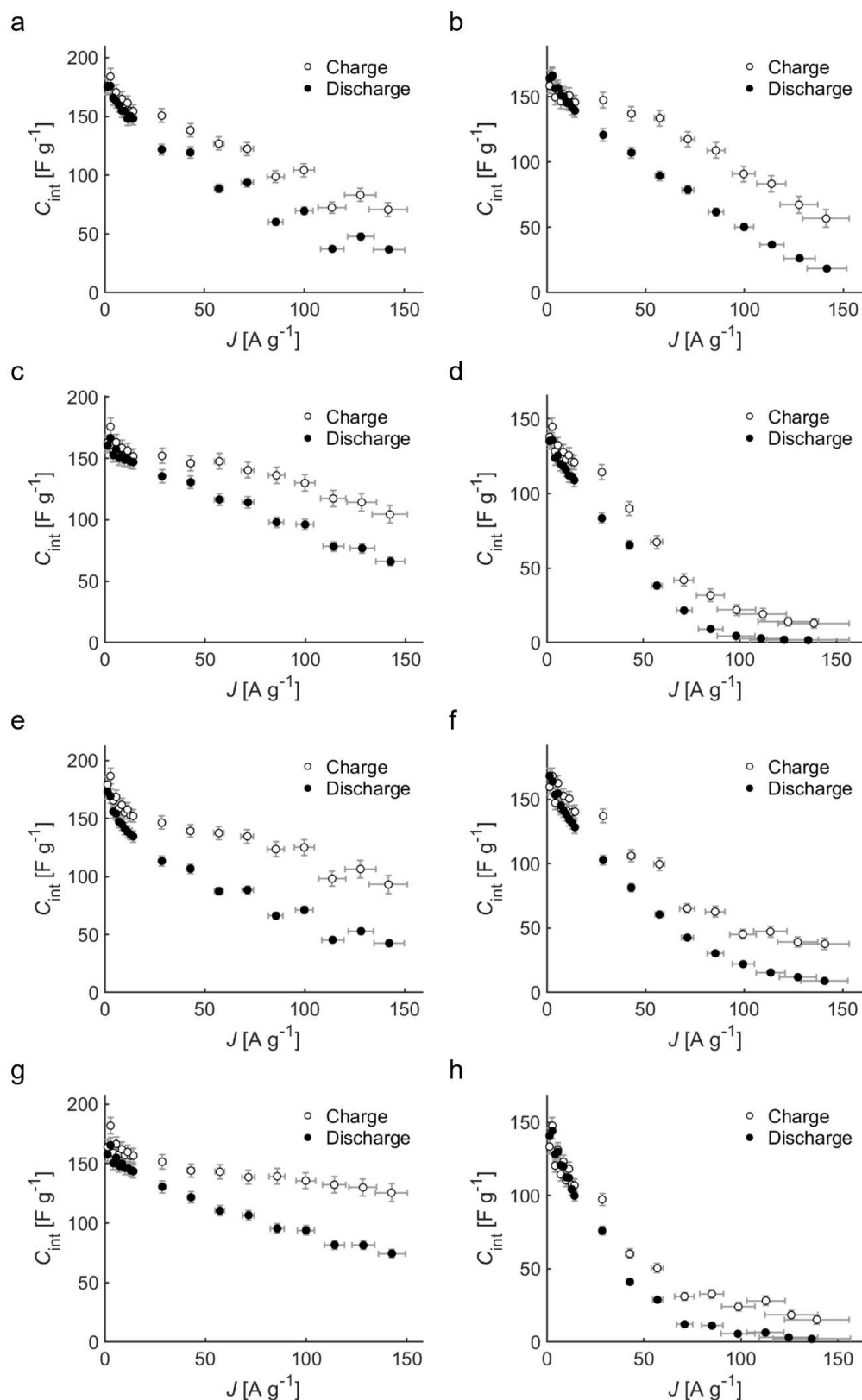
Figure 7. Influence of current density, J, on the estimated specific integral capacitance, C_{int}, of Na-B (a and b), K-B (c and d), Na-A (e and f) and K-A (g and h) during charging and discharging, both before (a, c, e and g) and after (b, d, f and h) subjecting the systems to 2,000 successive GCD cycles at 28.6 A g^{-1}.

ChemElectroChem

Research Article
doi.org/10.1002/celc.202300210

Chemistry
Europe
European Chemical
Societies Publishing

The effects of guest cation type on $Na_xK_yMnO_z$ storage characteristics depend on a complex interplay of factors including ion-transport kinetics, the thermodynamics of ion interactions with the host material, and the influence of guest ions on the dimensions of interstitial channels. In order to better understand differences between the C_{int} characteristics displayed in Figure 7, it is therefore prudent to address each stage of the pseudocapacitance mechanism in turn. In the hydrated state, K^+ ions exhibit greater conductivity (73.5 $S\,cm^2\,mol^{-1}$ at 25 °C) than their Na^+ counterparts (50.1 $S\,cm^2\,mol^{-1}$ at 25 °C),[13,48,51,82] enabling more rapid diffusion towards the $Na_xK_yMnO_z$ surface. Upon entering the host framework during a discharge cycle, K^+ ions can more readily shed the solvation shell of coordinating water molecules as they possess a relatively low enthalpy of hydration compared with the Na^+ case.[48–50] The resulting bare K^+ ions have a lower charge density than Na^+ ions and consequently experience weaker electrostatic attraction to the MnO_6 octahedra, resulting in a smaller activation barrier for deintercalation and less contraction of the diffusion pathways.[26,30,31,48–50] Furthermore, pre-insertion of alkali metal ions improves the electronic conductivity of $Na_xK_yMnO_z$ with respect to pristine MnO_2 by enhancing the Mn 3d and O 2p density of states close to the Fermi level,[14,33,45,50] and density functional theory (DFT) predicts that K^+ insertion promotes this phenomenon to a greater extent than Na^+ intercalation.[14,45,50] Although the pseudocapacitive behaviors of as-prepared K-B and K-A electrodes were well-matched by Na-B and Na-A at current densities on the order of 10 $A\,g^{-1}$, these considerations provide a plausible explanation for the superior performance of K-based systems at higher current densities, where storage processes are more significantly hindered by underlying kinetic limitations.

Whilst undergoing the sequence of 2,000 galvanostatic cycles, K-B and K-A experienced more rapid capacitance decay than their Na-based equivalents. Given the comparatively high mobility of K^+ ions, it is ostensibly paradoxical that K-mediated storage mechanisms were more susceptible to cycling-induced disruption than corresponding processes involving Na^+ ions; however, several factors could be responsible for this finding. For instance, the radius of a bare K^+ ion (1.4 Å) is significantly larger than in the Na^+ case (1.0 Å),[30,45,51,52,54,83] causing it to encounter greater steric hindrance and a larger energy barrier for diffusion[50,54] after removal of the hydration shell. Charge exchange with the MnO_6 octahedra is similarly impeded by the size of K^+ ions, resulting in fewer accessible electroactive sites for intercalation;[47] again, this effect is likely to be exacerbated by degradation of the $Na_xK_yMnO_z$ lattice, with electroactive sites depleted by the collapse of interstitial channels or material loss through disproportionation and subsequent dissolution of Mn-(III) species.[29,30] Finally, since the electrostatic forces between guest K^+ ions and MnO_6 octahedra are inherently weaker than corresponding Na^+ interactions, it follows that K^+ pre-insertion cannot counteract structural disintegration as effectively as the pre-intercalation of Na^+ ions.[15,29,32–36]

Due to competition between the properties that caused enhanced capacitance fading in K-B and K-A and the compensating factors that enabled these materials to outperform Na-B and Na-A in their as-prepared states, the relative storage characteristics of Na- and K-based electrodes are liable to vary between studies due to disparate synthesis and testing protocols. For example, whilst various investigations have demonstrated that K^+ insertion/extraction affords greater capacitance and Coulombic efficiency than intercalation/deintercalation of Na^+ ions,[14,31,45,48–50] others showcase the opposite trend.[11,25,46,47,51–53] Similarly, the superior capacitance retention of K-mediated systems in some reports[31,45,48] is countered by alternative publications wherein K^+ intercalation yielded similar or inferior cycling stability to the Na^+ case.[14,30,46,50,53] These literature disagreements highlight the clear need for research that rigorously addresses the benefits and pitfalls of $Na_xK_yMnO_z$ products using a self-consistent approach, rather than relying on comparisons between potentially incompatible studies.

Returning to the relationships depicted in Figure 7 and Figure S16, it is apparent that the crystallographic structure of the as-prepared materials had a lesser impact on storage behaviors than the nature of intercalating cations: the C_{int} vs J and η_Q vs J trends of the as-prepared Na-B and K-B electrodes closely resemble those of Na-A and K-A, respectively, whilst the post-cycling storage characteristics of the acid-synthesized products are only fractionally inferior to corresponding relationships from their basic counterparts. This similarity between the electrochemical properties of the birnessite and cryptomelane systems is potentially surprising given that the BET specific surface areas of Na-A and K-A were an order of magnitude greater than in the birnessite samples (Table 1). However, it should be recognized that specific surface area estimates derived from nitrogen adsorption isotherms are not representative of the area that is accessible to intercalating cations, which experience greater steric hindrance than nitrogen molecules and are also obstructed by electrode additives such as the ethyl cellulose binder layer. Indeed, research has shown that there is little correlation between the specific capacitance and surface area of $Na_xK_yMnO_z$ systems, even when comparing products with the same crystallographic phase.[41–43] Analogous to the contradictions between literature comparisons of Na- and K-intercalated materials, existing studies deliver varying conclusions regarding the relative electrochemical attributes of comparable α-MnO_z and δ-MnO_z products: some works indicate that the superior specific surface area afforded by cryptomelane structures is the primary determining factor in overall storage performance,[40,41,44] whereas others suggest that the birnessite phase offers superior capacitance,[22,37–39,42] likely due to the availability of wider ion passages than in the cryptomelane case.[8]

Equivalent Circuit Modelling

When discussing the GCD behaviors of the electrodes, it was noted that the instantaneous step-change in potential at a charge-discharge transition scales in direct proportion to the ESR of the pseudocapacitive system. However, the true magnitude of this resistance is difficult to determine accurately due to the finite time required for electrochemical instrumenta-

ChemElectroChem

Research Article
doi.org/10.1002/celc.202300210

Chemistry Europe
European Chemical
Societies Publishing

tion to reverse the direction of the applied current. In the case of a linear GCD relationship, an alternative strategy is to estimate the ESR by extrapolating the E vs t trend back to the charge-discharge transition,[81] but this approach is complicated by a transient non-linear phase associated with the "equivalent distributed resistance" (EDR) caused by charge redistribution through surface electrode pores.[76,81] Another problem with estimating the ESR from GCD measurements is that it fundamentally represents an intricate combination of Ohmic, charge-transfer and diffusion-borne resistances; hence, the practice of determining a single characteristic resistance value is implicitly predicated on an unrealistic assumption that the system can be approximated as a series configuration of a resistor and an ideal capacitor.

A more reliable way to investigate the impedance properties of a storage electrode is electrochemical impedance spectroscopy (EIS), which enables the various contributions of resistance and capacitance phenomena to be distinguished from relationships between the real and imaginary components of impedance, Z, and the frequency, f, of applied potential perturbations.[84] EIS characterization is typically performed at the measured open-circuit potential of the working electrode, as this value corresponds to equilibrium between oxidation and reduction reactions of electrolyte species at the electrode surface, where the Butler-Volmer equation for redox processes is approximately linear.[85] However, open-circuit potential measurements recorded prior to every CV experiment reveal that this equilibrium scenario did not occur at a consistent potential value over the course of electrochemical testing: open-circuit potential values in the range 0.21–0.76 V vs Ag|AgCl (3 M KCl) were exhibited by the four electrodes, possibly due to cyclical variations in the average Mn oxidation state and the changing concentrations of intercalated Na^+ and K^+ ions.[30,86] To overcome this difficulty, EIS was instead conducted at two widely separated bias potentials within the electrochemical stability window, 0.0 V and 0.5 V vs Ag|AgCl (3 M KCl), thereby enabling impedance behaviors of each system to be assessed as a function of the applied potential. Indeed, it has been acknowledged elsewhere that since the equivalent circuit components of supercapacitor systems are commonly voltage-dependent, the practice of conducting EIS exclusively at the open-circuit potential is liable to restrict the information that can be gleaned from the technique.[87]

Using EIS data acquired at a base potential of 0.5 V vs Ag|AgCl (3 M KCl) (Figure 8), Nyquist (Figure 8a and b) and Bode-magnitude (Figure 8c and d) plots were constructed to develop equivalent circuits for the systems both before (Figure 8a and c) and after (Figure 8b and d) they underwent 2,000 galvanostatic cycles at 28.6 A g^{-1}; corresponding plots yielded by EIS measurements obtained at 0.0 V vs Ag|AgCl (3 M KCl) are supplied in the Supporting Information (Figure S17). Each dataset was modelled using a modified Randles equivalent circuit[88–94] (Figure 8e and Figure S17e) composed of an Ohmic series resistance, R_s, equal to the sum of electrode and electrolyte resistance, a resistance R_{ct} and capacitance C_{ct} to account for pseudocapacitive charge transfer resulting from cation intercalation/deintercalation, and a constant phase element, Q_{dl}, to approximate the non-ideal capacitive behavior of electrostatic double-layers at the electrode surface. The latter contribution has a complex impedance given by Equation 5,[88]

$$Z_{dl} = \frac{1}{Q_{dl}(i\omega)^n} \tag{5}$$

where ω denotes the angular frequency of potential perturbations, and n is a constant that equals one in the case of an ideal capacitor. Finally, a Warburg impedance element, Z_W, describes slow diffusion-controlled ion transport to electro-active sites via passivating surface layers such as the ethyl cellulose polymer binder. Over the practical frequency range of the EIS experiments, Z_W obeys the Cottrell equation (Equation 6),[26,88]

$$Z_W = \frac{\sigma_W}{\sqrt{i\omega}} = \frac{\sigma_W}{\sqrt{2\omega}}(1-i) \tag{6}$$

where σ_W is a constant known as the Warburg coefficient. It can be shown that σ_W is inversely proportional to the square root of the diffusion constant for charged species travelling to and from the electrode surface, and hence it serves as a useful indicator of ion mobility. Estimates of the equivalent circuit parameters for the as-prepared systems are compiled in Table 3 and Table S1 of the Supporting Information, which correspond to bias potentials of 0.5 V and 0.0 V vs Ag|AgCl (3 M KCl), respectively. Similarly, post-cycling fitting values obtained from EIS data acquired at 0.5 V and 0.0 V vs Ag|AgCl (3 M KCl) are collated in Table 4 and Table S2 of the Supporting Information, respectively.

A noteworthy feature of the applied equivalent circuit model is that it uses a single ideal capacitance, C_{ct}, to simulate the pseudocapacitive characteristics of a given $Na_xK_yMnO_z$ system. Nevertheless, the generated fitting functions provide an

Table 3. Pre-cycling estimates of the Ohmic series resistance, R_s, charge-transfer resistance, R_{ct}, charge-transfer capacitance, C_{ct}, Warburg coefficient, σ_W, electric double-layer capacitance, Q_{dl}, and the constant phase element parameter n, obtained by modelling EIS measurements acquired at a bias potential of 0.5 V vs Ag|AgCl (3 M KCl); all gravimetric variables are normalized with respect to the estimated mass of $Na_xK_yMnO_z$.

Parameter	Na-B	K-B	Na-A	K-A
R_s [Ω mg]	0.51	0.49	0.54	0.38
R_{ct} [Ω mg]	2.4	1.5	2.4	1.1
C_{ct} [F g^{-1}]	150	140	120	130
σ_W [Ω mg s$^{-1/2}$]	3.8	3.2	3.0	2.6
Q_{dl} [F s^{n-1} g^{-1}]	6.9	1.6	2.8	1.5
n	0.70	0.80	0.76	0.83
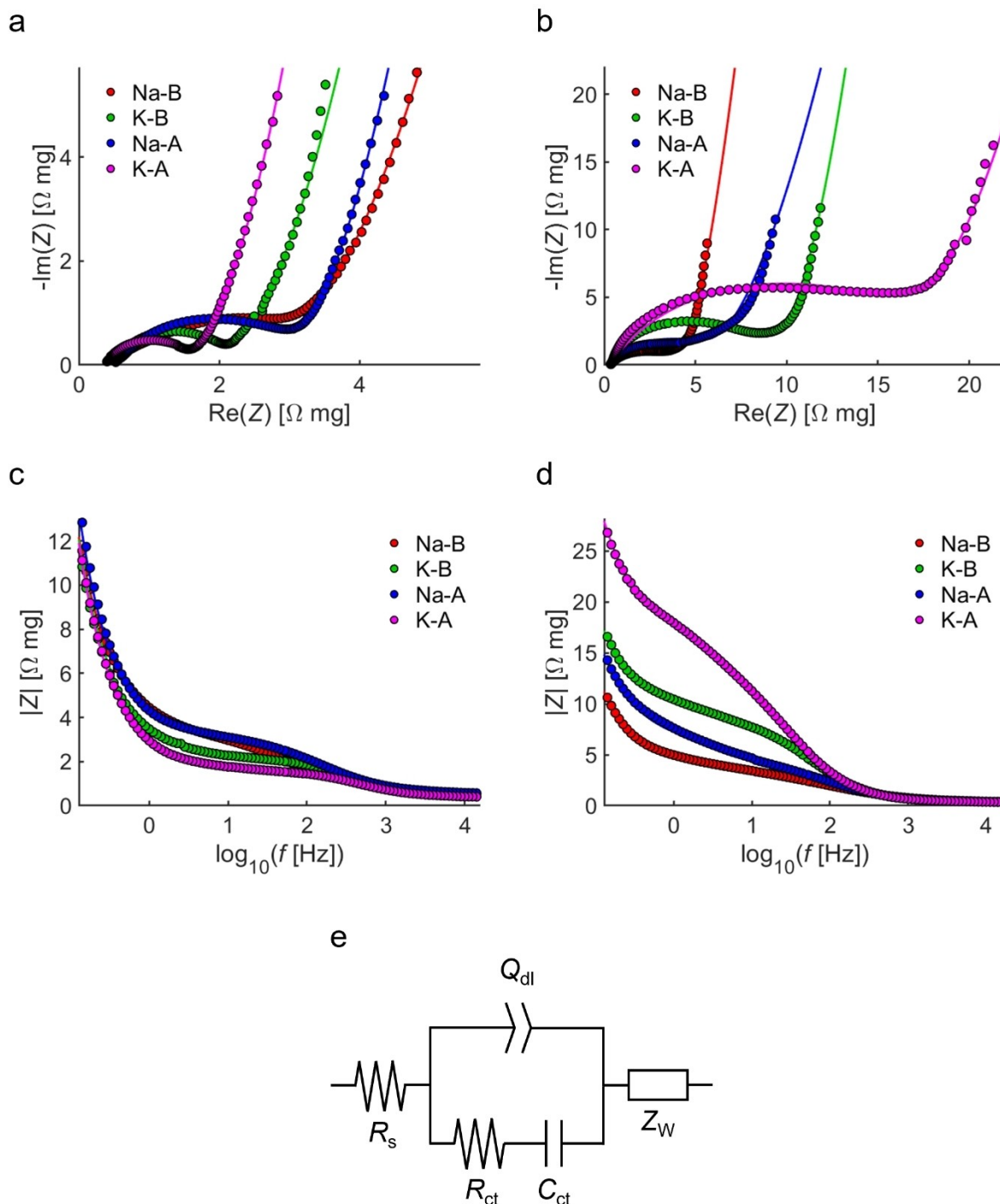
Figure 8. Nyquist (a and b) and Bode-magnitude (c and d) plots constructed from EIS measurements at a bias potential of 0.5 V vs Ag|AgCl (3 M KCl), acquired before (a and c) and after (b and d) subjecting the electrodes to 2,000 GCD cycles at 28.6 A g^{-1}. Fitting functions were generated using a modified Randles equivalent circuit model (e) comprising impedance contributions from: Ohmic series resistances, R_s, in the electrodes and electrolyte; charge-transfer resistances, R_{ct}, at the interface between electrode and electrolyte; a capacitance, C_{ct}, resulting from intercalation/deintercalation processes; a constant phase element, Q_{dl}, corresponding to electric double-layer capacitance; and a Warburg impedance element, Z_W, describing diffusion-controlled ion transport.

accurate representation of pre-cycling measurements, indicating that this simplification is indeed appropriate due to the fast kinetics of intercalation/deintercalation mechanisms. It is instructive to recall that the rapidity of cation insertion/extraction is also evident from corresponding pre-cycling low-v CV (Figure 5a, c, e and g) and low-J GCD (Figure 6a, c, e and g)

trends, which bear a close resemblance to the ideal rectangular CV and linear GCD relationships of a classic capacitor. By contrast, slow, diffusion-controlled storage phenomena would manifest as distinct peaks in the cyclic voltammograms and plateaus in the GCD traces,[76] but no such features appear in any of the pre-cycling CV or GCD datasets. The model is further

Table 4. Post-cycling estimates of the Ohmic series resistance, R_s, charge-transfer resistance, R_{ct}, charge-transfer capacitance, C_{ct}, Warburg coefficient, σ_W, electric double-layer capacitance, Q_{dl}, and the constant phase element parameter n, obtained by modelling EIS measurements acquired at a bias potential of 0.5 V vs Ag|AgCl (3 M KCl); all gravimetric variables are normalized with respect to the estimated mass of $Na_xK_yMnO_z$.

Parameter	Na-B	K-B	Na-A	K-A
R_s [Ω mg]	0.31	0.35	0.33	0.32
R_{ct} [Ω mg]	3.6	8.7	5.2	16.0
C_{ct} [F g^{-1}]	160	130	170	110
σ_W [Ω mg s$^{-1/2}$]	2.5	4.0	5.5	7.9
Q_{dl} [F s^{n-1} g^{-1}]	4.9	2.0	5.3	2.5
n	0.70	0.77	0.70	0.75

validated by the parameter C_{ct}, which, in line with the magnitudes of C_{int} estimates derived from GCD measurements (Figure 7), mostly adopts values in the range 100–200 F g^{-1}. When comparing C_{ct} and C_{int} in this way, it is important to acknowledge that the form of each EIS fitting function is not significantly sensitive to small changes (on the order of 10%) in the variables C_{ct}, Q_{dl} and σ_W, and hence these quantities are constrained to an accuracy of two significant figures in Table 3 and Table 4, and in Table S1 and Table S2 of the Supporting Information. Whilst the equivalent circuit model generates marginally inferior descriptions of the post-cycling EIS data, most noticeably in the case of Na-A, it nevertheless provides useful indicative parameter estimates for the purpose of investigating the origins of capacitance decay.

From the near-convergence of the high-frequency x-intercepts in the Nyquist plots (Figure 8a and b, and Figure S17a and b), Ohmic resistance was evidently affected little by compositional and crystallographic differences between the four $Na_xK_yMnO_z$ materials. However, at both 0.0 V and 0.5 V vs Ag|AgCl (3 M KCl), R_s was found to decrease over the course of electrochemical testing, which is possibly attributable to gradual penetration of the electrode films by surrounding electrolyte. As apparent from the relative diameters of the semicircular sections of the Nyquist plots, K-B and K-A offered significantly less resistance to charge transfer processes than Na-B and Na-A in the as-prepared state, but they also experienced greater increases in R_{ct} during prolonged testing. Charge transfer was similarly influenced by crystallographic phase: the birnessite materials, Na-B and K-B, exhibited higher initial R_{ct} values than their cryptomelane counterparts at both bias potentials, but they delivered lower R_{ct} values after the GCD cycling process. With the notable exception of Na-B, enhanced charge-transfer resistance during GCD cycling was accompanied by a corresponding increase in σ_W, which signifies a diminished rate of ion diffusion between the electrolyte and electroactive surface sites.

The pre- and post-cycling variations of R_{ct} are qualitatively consistent with results from the GCD tests, wherein it was shown that the as-prepared Na-B and Na-A systems delivered fractionally lower values of C_{int} at given J than K-B and K-A (Figure 7a, c, e and g, and Table 2), despite displaying greater post-cycling capacitances (Figure 7b, d, f and h, and Table 2). The R_{ct} trends also align with the $|J(0.5\,V)|/\nu^{1/2}$ vs $\nu^{1/2}$ relationships acquired from CV data (Figure S12): in comparison to K-B and K-A, the post-cycling $|J(0.5\,V)|/\nu^{1/2}$ vs $\nu^{1/2}$ variations of Na-B

and Na-A more closely resemble their pre-cycling behaviors, implying that they were less significantly impacted by the cycling procedure. From these arguments it follows that changes in R_{ct} are strongly linked to performance deterioration during GCD cycling, characterized by decreases in C_{int} and η_Q, and diminished linearity of the J vs ν relationship. In this regard, Na$^+$ insertion/extraction ostensibly had a weaker destabilizing influence than the intercalation/deintercalation of K$^+$ ions, whilst δ-MnO$_z$ showcased greater cycling stability than α-MnO$_z$.

Conclusions

To explore the effects of synthesis precursor concentrations on the morphology, composition and electrochemical properties of co-precipitated $Na_xK_yMnO_z$ products, sample materials formulated at two different pH values with an abundance of either Na$^+$ or K$^+$ cations were studied using a combination of characterization techniques. Through these investigations it was demonstrated that:

- Acidic synthesis conditions (pH 1.7) favor the formation of cryptomelane (α-MnO$_z$) nanorods, whereas basic solutions (pH 12.3) preferentially yield a turbostratic birnessite (δ-MnO$_z$) product composed of agglomerated nanoflakes with randomly ordered lattice planes.
- Hydroxide ions in the synthesis solution suppress reduction of Mn^{4+} ions to the 3+ oxidation state, with δ-MnO$_z$ materials exhibiting an O/Mn atomic ratio close to two, as expected for pristine MnO$_2$.
- Intercalation/deintercalation of alkali metal cations occurs more readily in the interlayer channels of δ-MnO$_z$ than the one-dimensional tunnel structure of α-MnO$_z$, enabling the former to achieve higher Na/Mn and K/Mn atomic ratios than their α-MnO$_z$ equivalents.
- Variations in specific integral capacitance and cycling stability correlate with charge-transfer resistance: materials with no Na content initially exhibited higher capacitances and lower charge-transfer resistances than $Na_xK_yMnO_z$ products from a Na-rich environment, yet the K-only electrodes became more resistive to charge transfer than Na-based systems during prolonged GCD cycling, culminating in inferior post-cycling capacitance and Coulombic efficiency.
- Crystallographic phase has a weaker influence than cation type on the electrochemical characteristics of as-prepared $Na_xK_yMnO_z$ electrodes. Comparing α-MnO$_z$ and δ-MnO$_z$

ChemElectroChem

Research Article
doi.org/10.1002/celc.202300210

Chemistry Europe
European Chemical
Societies Publishing

products intercalated by the same type of principal guest cation, pre-cycling differences between the specific integral capacitances of the two polymorphs were of similar magnitude to the experimental uncertainties.

- In comparison to equivalent α-MnO_z materials, the δ-MnO_z phase is less vulnerable to electrochemical performance deterioration during prolonged GCD cycling.

Combining these findings, charge-transfer resistance is identified as the primary source of performance loss during prolonged cycling, and it is reasoned that K^+ intercalation/deintercalation has a stronger destabilizing effect on capacitance and Coulombic efficiency than the insertion/extraction of Na^+ ions. In addition, the kinetics of cation intercalation/deintercalation into birnessite δ-MnO_z were shown to be less sensitive to GCD cycling than in cryptomelane α-MnO_z, as evidenced by the evolution of charge-transfer resistance in these materials. It therefore follows that the long-term storage performance and cycling stability of a $Na_xK_yMnO_z$ electrode may be maximized by selecting a birnessite product with Na^+ as the predominant guest cation, despite K-based systems offering marginally superior storage capabilities in the initial stages of electrochemical testing.

Whilst a plethora of research has addressed the effects of guest cations and crystallographic phase on the electrochemical properties of $Na_xK_yMnO_z$, studies have hitherto provided insufficient detail regarding the effects of prolonged testing on storage performance. By evaluating the relationships between storage parameters both before and after subjecting $Na_xK_yMnO_z$ electrodes to thousands of GCD cycles, the present work overcomes this limitation of existing investigations by providing a more comprehensive understanding of how storage performance is influenced by crystallography, morphology and the nature of intercalating species. Furthermore, competitive electrode characteristics have been attained via a scalable, low-temperature synthesis strategy and environmentally sustainable, low-toxicity materials such as an ethyl cellulose (an inexpensive, non-toxic and environmentally sustainable polymer binder[95,96]). In these ways, the present investigation provides a useful platform for additional development and optimization of $Na_xK_yMnO_z$ materials, as well as informing further research into areas such as the interplay between crystallographic phase and cation pre-insertion, and the physical origins of capacitance decay during cycling.

Experimental Section

Reagents and Materials: All chemicals employed in this work were of analytical grade and were used as received. Manganese(II) sulfate monohydrate ($MnSO_4.H_2O$, $\geq 99\%$), potassium permanganate ($KMnO_4$, $\geq 99.0\%$), sodium sulfate (Na_2SO_4, $\geq 99.0\%$), potassium sulfate (K_2SO_4, $\geq 99.0\%$), sodium hydroxide (NaOH, $\geq 98\%$), potassium hydroxide (KOH, $\geq 85\%$) and 4-hydroxy-4-methyl-2-pentanone (99%) were acquired from Sigma-Aldrich Ltd., whilst ethyl cellulose (48.0–49.5% ethoxyl content), Super P carbon black ($\geq 99\%$), nickel foil (99.5%, 0.25 mm thickness) and platinum wire ($\geq 99.99\%$, 0.5 mm diameter) were obtained from Fisher Scientific Ltd.

Synthesis of $Na_xK_yMnO_z$: For the gram-scale synthesis of $Na_xK_yMnO_z$, a 400 mL aqueous solution of Mn_2SO_4 (100 mM), $KMnO_4$ (67 mM), and either Na_2SO_4 or K_2SO_4 (400 mM) was prepared by sequentially combining separate solutions of each precursor, with the $KMnO_4$ solution introduced as the final reagent. In an alkaline synthesis process, the pH of the solution was subsequently adjusted to 12.3 under constant stirring through the dropwise addition of aqueous NaOH or KOH (1.0 M), yielding a final added volume of between 104 mL and 113 mL; the cation in the hydroxide base was chosen to match the cation present in the sulfate salt. To obtain a pH 1.7 precursor solution, 104 mL of deionized water was instead added to the original 400 mL volume in place of the NaOH or KOH solution. In both synthesis routes, the final pH of the solution was measured using a Mettler Toledo FiveGo F2 pH probe. With continuous stirring, the combined solution was then heated under reflux for 12 hours at 75 °C in a thermocouple-controlled silicone oil bath. The resulting suspension was allowed to cool naturally to room temperature before being centrifuged several times with deionized water in order to remove residual reagents from the $Na_xK_yMnO_z$ precipitate. Finally, the product was redispersed in acetone and dried in a muffle furnace at 60 °C.

Phase Identification: The crystallographic structures of the $Na_xK_yMnO_z$ products were determined by transmission-mode powder X-ray diffractometry (XRD) using a Bruker D8 Advance X-ray diffractometer. The instrument was equipped with Cu–Kα irradiation and a nickel filter, and it was set to operate at an X-ray power of 1,600 W (40 V × 40 A); measurements were recorded over a 2θ range of 5–90°, with a dwell time of 15 s and 2θ increments of 0.025° between steps, and each sample powder was rotated at 30 rpm inside a special glass capillary with a 0.7 mm outside-diameter.

Morphology Investigations: Examinations of product morphology were carried out via a combination of field-emission scanning electron microscopy (SEM), transmission electron microscopy (TEM) and scanning transmission electron microscopy (STEM). For SEM, a Hitachi S-4800 instrument was employed with emission voltage and current settings of 10 kV and 10 µA, respectively, and each sample powder was pressed onto an adhesive carbon tab. A FEI Talos F200X system was used to perform TEM and STEM at an accelerating voltage of 200 kV, for which each sample was prepared by first introducing a small quantity of the product (less than 0.1 mg) into a 1:1 v/v mixture of isopropanol and methanol, before agitating the suspension in an ultrasonic bath and then transferring it dropwise onto a 300-mesh lacey carbon-coated copper grid. Where possible, lattice d-spacings were estimated from TEM images by applying ImageJ software to obtain distance measurements over a minimum of ten lattice planes.

Composition Analysis: The surface chemical composition of each material was estimated through deconvolution of X-ray photoelectron spectroscopy (XPS) measurements acquired using a Kratos Axis Supra system, which was fitted with a monochromated Al–Kα source operating at an emission current of 15 mA. For these characterizations, a Retsch PP 25 pellet press was employed in conjunction with a Specac pellet die to compress the $Na_xK_yMnO_z$ products into pellets of 5 mm diameter, and data were collected from four 700 µm × 300 µm rectangular locations across the pellet-ized sample surface. In each case, survey spectra were recorded over binding energies between −5 eV and 1,350 eV, with a dwell time of 100 ms, 160 eV pass energy, and 1 eV energy increments. Higher resolution scans of core photoelectron peaks were subsequently obtained using a dwell time of 1 s, 20 eV pass energy and 50 meV energy increments. Throughout all measurements, electronic charge neutralization was applied with a charge balance potential of 3.3 V, and a filament bias and current of 1.0 V and

ChemElectroChem

Research Article
doi.org/10.1002/celc.202300210

Chemistry Europe
European Chemical
Societies Publishing

0.4 A, respectively. Additional information regarding XPS data interpretation is supplied in the Supporting Information.

Surface Area Measurement: The Brunauer-Emmett-Teller (BET) surface area, S_{BET}, of each product was estimated from the nitrogen adsorption curve of a 0.27–0.66 g powder sample, as measured using a TriStar II 3020 surface area and porosity analyser; prior to BET analysis, the powders were degassed under vacuum by the instrument at 120 °C for one day. A comprehensive overview of the BET analysis procedure is included in the Supporting Information.

Electrode Preparation: In order to improve electron conductivity between $Na_xK_yMnO_z$ particles, viscous slurries composed of the synthesized $Na_xK_yMnO_z$ powder, Super P carbon black and ethyl cellulose in 4-hydroxy-4-methyl-2-pentanone were prepared, with the solid constituents present in a mass-ratio of 7:2:1, respectively; each slurry had a ca. 5:1 mass-ratio of liquid to solid constituents. Mixing was carried out using a Thinky ARE-250 planetary mixer, operated in five-minute steps at a rotational velocity of 2,000 rpm; this blending process was conducted over a minimum of two steps after combining the slurry components, with a further mixing step performed immediately prior to coating. All mixtures were allowed to age overnight before use. Each slurry was deposited over a rectangular 40 mm×15 mm area of nickel foil (100 mm×20 mm×0.25 mm) by tape-casting with a glass rod, before allowing the film to dry naturally in air.

To decrease the risk of delamination during electrochemical testing, the cathode films were pressed between PTFE-coated heating sheets using a Devil Press S15 hydraulic press for 15 minutes at an estimated pressure of 7.5 MPa and a temperature of 120 °C; a piezoelectric CBES button load cell was employed to construct a linear calibration plot for the press. The total film mass after pressing was measured by subtracting the mass of the uncoated nickel substrate from the final coated mass, using a mass balance with a stated precision of 0.1 mg. The electrodes investigated herein had a measured film mass in the range 2.6–2.8 mg, which translates to 0.30–0.33 mg cm^{-2} of electroactive material, assuming that the film components were distributed homogeneously throughout the coated slurry. Finally, uncoated areas of the nickel substrate were masked with a UV-curing Solarez epoxy resin, which was hardened at a peak wavelength of 302 nm by a Thermo Scientific Pierce 3UV lamp with a stated power density of 2.8 mW cm^{-2}. A schematic illustrating the electrode preparation sequence is provided in the Supporting Information (Figure S18).

Electrochemical Testing: An Ivium-n-Stat electrochemical station was used to characterize each $Na_xK_yMnO_z$ working electrode in a three-electrode configuration containing a platinum coil counter electrode, an Ag|AgCl (3 M KCl) reference electrode, and an electrolyte of aqueous Na_2SO_4 or K_2SO_4 (0.5 M), selected so that the cation matched the predominant alkali metal ion present during synthesis. Prior to testing, dissolved oxygen was expelled from the electrolyte by sparging with nitrogen gas for two hours at a flow rate of 0.5 L min^{-1}, and the electrode was allowed to stabilize in the de-aerated electrolyte for a minimum of one hour at open-circuit. Electrochemical storage properties were subsequently investigated using a combination of cyclic voltammetry (CV), galvanostatic charge-discharge (GCD) cycling and electrochemical impedance spectroscopy (EIS). Throughout the present study, gravimetric variables such as specific capacitance and specific current density are normalized with respect to the estimated mass of $Na_xK_yMnO_z$ within the electrode film, invoking an assumption of slurry homogeneity to approximate the mass of $Na_xK_yMnO_z$ as 70% of the measured film mass.

CV experiments were conducted over five cycles between 0.0 V and 1.0 V vs Ag|AgCl (3 M KCl) at potential scan rates in the range 10–1,000 mV s^{-1}; the first cycle of each CV dataset was commenced at the open-circuit potential of the system, which was measured prior to cycling for a period of five minutes. Analysis of the CV data was performed by addressing measurements from the fifth cycle of each CV procedure. When utilizing Dunn's formula (Equation 4), the magnitude of current J, $|J|$, was taken as the mean of the two $|J|$ values yielded by the oxidative and reductive sections of a given cyclic voltammogram, and the uncertainty in $|J|$ was approximated as half the difference between these values. GCD measurements were carried out over two consecutive cycles between 0.0 V and 1.0 V vs Ag|AgCl (3 M KCl) at current densities ranging from 1.43 A g^{-1} to 143 A g^{-1}, with all electrochemical parameters estimated from the second charge-discharge cycle. In both CV and GCD sequences, tests were carried out in staggered order so that any systematic drift could be quantified from step-changes within the measured trends. EIS data were generated over a frequency range of 100 kHz to 0.1 Hz at DC bias potentials of 0.0 V and 0.5 V vs Ag|AgCl (3 M KCl), applying AC potential oscillations with a peak-to-peak amplitude of 10 mV. Electrode durability was evaluated by repeating the same sequence of CV, GCD and EIS procedures after performing 2,000 GCD cycles at 28.6 A g^{-1}; prior to commencing these post-cycling CV, GCD and EIS experiments, the electrolyte was replaced with a fresh batch of $Na_2SO_{4(aq)}$ or $K_2SO_{4(aq)}$ (0.5 M) solution, which was again sparged with a 0.5 L min^{-1} flow of nitrogen gas for two hours prior to use. The Supporting Information contains further details about the protocol used to obtain specific integral capacitance estimates from the GCD measurements.

Supporting Information

Supporting Information is available from the Wiley Online Library or from the author. Additional references are cited within the Supporting Information.[66,70,74–76,97]

Competing Interests

Author Kittiwat Kamlungsua is employed by Enserv Power Co. Ltd, which part-funded the research. The authors have no other potential conflicts of interest to declare.

Data Availability Statement

The data that support the findings of this study are available from the corresponding author upon reasonable request.

[1] B. Babu, P. Simon, A. Balducci, *Adv. Energy Mater.* **2020**, *10*, e2001128.
[2] W. Jing, C. H. Lai, W. S. H. Wong, M. L. D. Wong, *Sustain. Energy Technol. Assess.* **2017**, *22*, 55–64.
[3] T. M. Narayanan, Y. G. Zhu, E. Gençer, G. McKinley, Y. Shao-Horn, *Joule* **2021**, *5*, 2934–2954.
[4] A. J. Hurd, R. L. Kelley, R. G. Eggert, M. H. Lee, *MRS Bull.* **2012**, *37*, 405–410.
[5] J. Xie, Z. Liang, Y. C. Lu, *Nat. Mater.* **2020**, *19*, 1006–1011.
[6] M. Toupin, T. Brousse, D. Bélanger, *Chem. Mater.* **2004**, *16*, 3184–3190.
[7] W. Guo, C. Yu, S. Li, Z. Wang, J. Yu, H. Huang, J. Qiu, *Nano Energy* **2019**, *57*, 459–472.
[8] R. Samal, B. Chakraborty, C. S. Rout, *J. Appl. Phys.* **2019**, *126*, e045112.
[9] S. K. Ghosh, *ACS Omega* **2020**, *5*, 25493–25504.
[10] H. Bai, S. Liang, T. Wei, Q. Zhou, M. Shi, Z. Jiang, J. Feng, M. Zhang, Z. Fan, *J. Power Sources* **2022**, *523*, e231032.
[11] Q. Ye, R. Dong, Z. Xia, G. Chen, H. Wang, G. Tan, L. Jiang, F. Wang, *Electrochim. Acta* **2014**, *141*, 286–293.
[12] H. Zhang, L. Wu, *J. Electrochem. Soc.* **2018**, *165*, 2815–2823.
[13] N. Zarshad, A. U. Rahman, J. Wu, A. Ali, F. Raziq, L. Han, P. Wang, G. Li, H. Ni, *Chem. Eng. J.* **2021**, *415*, e128967.
[14] L. Niu, L. Yan, Z. Lu, Y. Gong, T. Chen, C. Li, X. Liu, S. Xu, *J. Energy Chem.* **2021**, *56*, 245–258.
[15] N. Jabeen, Q. Xia, S. V. Savilov, S. M. Aldoshin, Y. Yu, H. Xia, *ACS Appl. Mater. Interfaces* **2016**, *8*, 33732–33740.
[16] Q. Chen, J. Chen, Y. Zhou, C. Song, Q. Tian, J. Xu, C. P. Wong, *Appl. Surf. Sci.* **2018**, *440*, 1027–1036.
[17] B. Xu, L. Yu, M. Sun, F. Ye, Y. Zhong, G. Cheng, H. Wang, Y. Mai, *RSC Adv.* **2017**, *7*, 14910–14916.
[18] M. Huang, Y. Zhang, F. Li, L. Zhang, R. S. Ruoff, Z. Wen, Q. Liu, *Sci. Rep.* **2014**, *4*, e3878.
[19] A. Xia, W. Yu, J. Yi, G. Tan, H. Ren, C. Liu, *J. Electroanal. Chem.* **2019**, *839*, 25–31.
[20] Y. Qian, C. Huang, R. Chen, S. Dai, C. Wang, *Int. J. Electrochem. Sci.* **2016**, *11*, 7453–7460.
[21] R. Su, H. Wang, Y. Sun, P. Guo, *Colloids Surf. A* **2021**, *609*, e125579.
[22] R. A. Aziz, R. Jose, *J. Electroanal. Chem.* **2017**, *799*, 538–546.
[23] Z. Hu, X. Xiao, L. Huang, C. Chen, T. Li, T. Su, X. Cheng, L. Miao, Y. Zhang, J. Zhou, *Nanoscale* **2015**, *7*, 16094–16099.
[24] A. Adomkevicius, L. Cabo-Fernandez, T. H. Wu, T. M. Ou, M. G. Chen, Y. Andreev, C. C. Hu, L. J. Hardwick, *J. Mater. Chem. A* **2017**, *5*, 10021–10026.
[25] P. Y. Chen, A. Adomkevicius, Y. T. Lu, S. C. Lin, Y. H. Tu, C. C. Hu, *J. Electrochem. Soc.* **2019**, *166*, 1875–1883.
[26] C. J. Raj, R. Manikandan, P. Sivakumar, D. O. Opar, A. D. Savariraj, W. J. Cho, H. Jung, B. C. Kim, *J. Alloys Compd.* **2022**, *892*, e162199.
[27] X. Wang, Y. Wang, X. Zhao, *Crystals* **2022**, *12*, e115.
[28] R. Teimuri-Mofrad, E. Payami, A. Piriniya, R. Hadi, *Appl. Organomet. Chem.* **2022**, *36*, e6620.
[29] T. Liu, Y. Li, *InfoMat* **2020**, *2*, 807–842.
[30] D. Chen, D. Ding, X. Li, G. H. Waller, X. Xiong, M. A. El-Sayed, M. Liu, *Chem. Mater.* **2015**, *27*, 6608–6619.
[31] P. Xiong, R. Ma, N. Sakai, X. Bai, S. Li, T. Sasaki, *ACS Appl. Mater. Interfaces* **2017**, *9*, 6282–6291.
[32] Y. Liu, J. Xu, J. Li, Z. Yang, C. Huang, H. Yu, L. Zhang, J. Shu, *Coord. Chem. Rev.* **2022**, *460*, e214477.
[33] S. Zhu, Y. Wang, J. Zhang, J. Sheng, F. Yang, M. Wang, J. Ni, H. Jiang, Y. Li, *Energy Environ. Mater.* **2022**, *6*, e12382.
[34] C. Y. Tsai, T. S. Su, T. C. Wei, M. S. Wu, *Electrochim. Acta* **2022**, *430*, e141107.
[35] H. Dai, R. Zhou, Z. Zhang, J. Zhou, G. Sun, *Energy Mater.* **2022**, *2*, e200040.
[36] D. A. Kitchaev, S. T. Dacek, W. Sun, G. Ceder, *J. Am. Chem. Soc.* **2017**, *139*, 2672–2681.
[37] H. A. Pan, O. Ghodbane, Y. T. Weng, H. S. Sheu, J. F. Lee, F. Favier, N. L. Wu, *J. Electrochem. Soc.* **2015**, *162*, 5106–5114.
[38] A. A. Radhiyah, M. I. Izwan, V. Baiju, C. Kwok Feng, I. Jamil, R. Jose, *RSC Adv.* **2015**, *5*, 9667–9673.
[39] E. A. Arkhipova, A. S. Ivanov, K. I. Maslakov, R. Y. Novotortsev, S. V. Savilov, H. Xia, A. V. Desyatov, S. M. Aldoshin, *Ionics* **2022**, *28*, 3501–3509.
[40] S. Devaraj, N. Munichandraiah, *J. Phys. Chem. C* **2008**, *112*, 4406–4417.
[41] T. Brousse, M. Toupin, R. Dugas, L. Athouël, O. Crosnier, D. Bélanger, *J. Electrochem. Soc.* **2006**, *153*, 2171–2180.
[42] X. Bai, X. Tong, Y. Gao, W. Zhu, C. Fu, J. Ma, T. Tan, C. Wang, Y. Luo, H. Sun, *Electrochim. Acta* **2018**, *281*, 525–533.
[43] N. Li, X. Zhu, C. Zhang, L. Lai, R. Jiang, J. Zhu, *J. Alloys Compd.* **2017**, *692*, 26–33.
[44] A. Boisset, L. Athouël, J. Jacquemin, P. Porion, T. Brousse, M. Anouti, *J. Phys. Chem. C* **2013**, *117*, 7408–7422.
[45] Q. Xie, G. Cheng, T. Xue, L. Huang, S. Chen, Y. Sun, M. Sun, H. Wang, L. Yu, *Mater. Today Energy* **2022**, *24*, e100934.
[46] M. A. Desai, A. Kulkarni, G. Gund, S. D. Sartale, *Energy Fuels* **2021**, *35*, 4577–4586.
[47] N. Ma, S. Kosasang, A. Krittayavathananon, N. Phattharasupakun, S. Sethuraman, M. Sawangphruk, *Chem. Commun.* **2019**, *55*, 1213–1216.
[48] J. Shao, X. Li, Q. Qu, Y. Wu, *J. Power Sources* **2013**, *223*, 56–61.
[49] Q. Qu, P. Zhang, B. Wang, Y. Chen, S. Tian, Y. Wu, R. Holze, *J. Phys. Chem. C* **2009**, *113*, 14020–14027.
[50] J. Wan, X. Gu, P. Ji, J. Li, J. Lu, S. Luo, B. Li, L. Huang, M. He, C. Hu, *Appl. Phys. Lett.* **2021**, *119*, e163901.
[51] C. Xu, B. Li, H. Du, F. Kang, Y. Zeng, *J. Power Sources* **2008**, *184*, 691–694.
[52] F. Yi, Y. Huang, A. Gao, F. Zhang, D. Shu, W. Chen, H. Cheng, X. Zhou, R. Zeng, *Ionics* **2019**, *25*, 2393–2399.
[53] Y. Shi, M. Zhang, J. Zhao, L. Zhang, X. Cui, X. Zhu, D. Jin, J. Gong, D. Yang, J. Li, *Electron. Mater. Lett.* **2022**, *18*, 475–488.
[54] M. J. Young, A. M. Holder, S. M. George, C. B. Musgrave, *Chem. Mater.* **2015**, *27*, 1172–1180.
[55] N. Qiu, H. Chen, Z. Yang, S. Sun, Y. Wang, *Electrochim. Acta* **2018**, *272*, 154–160.
[56] M. F. L. Haris, C. Y. Yin, Z. T. Jiang, B. M. Goh, X. Chen, W. A. Al-Masry, A. M. Abukhalaf, M. El-Harbawi, N. M. Huang, H. N. Lim, *Ceram. Int.* **2014**, *40*, 1245–1250.
[57] J. Zhou, L. Yu, W. Liu, X. Zhang, W. Mu, X. Du, Z. Zhang, Y. Deng, *Sci. Rep.* **2015**, *5*, e17858.
[58] Y. Munaiah, B. G. S. Raj, T. P. Kumar, P. Ragupathy, *J. Mater. Chem. A* **2013**, *1*, 4300–4306.
[59] M. Villalobos, B. Lanson, A. Manceau, B. Toner, G. Sposito, *Am. Mineral.* **2006**, *91*, 489–502.
[60] B. Yin, S. Zhang, H. Jiang, F. Qu, X. Wu, *J. Mater. Chem. A* **2015**, *3*, 5722–5729.
[61] A. Zahoor, H. S. Jang, J. S. Jeong, M. Christy, Y. J. Hwang, K. S. Nahm, *RSC Adv.* **2014**, *4*, 8973–8977.
[62] A. Iyer, J. Del-Pilar, C. K. King'ondu, E. Kissel, H. F. Garces, H. Huang, A. M. El-Sawy, P. K. Dutta, S. L. Suib, *J. Phys. Chem. C* **2012**, *116*, 6474–6483.
[63] K. Chen, M. Wang, G. Li, Q. He, J. Liu, F. Li, *Materials* **2018**, *11*, e601.
[64] R. A. Davoglio, G. Cabello, J. F. Marco, S. R. Biaggio, *Electrochim. Acta* **2018**, *261*, 428–435.
[65] C. Tanggarnjanavalukul, N. Phattharasupakun, J. Wutthiprom, P. Kidkhunthod, M. Sawangphruk, *Electrochim. Acta* **2018**, *273*, 17–25.
[66] M. C. Biesinger, B. P. Payne, A. P. Grosvenor, L. W. M. Lau, A. R. Gerson, R. S. C. Smart, *Appl. Surf. Sci.* **2011**, *257*, 2717–2730.
[67] M. Wang, K. Chen, J. Liu, Q. He, G. Li, F. Li, *Catalysts* **2018**, *8*, e138.
[68] L. Yan, C. Shen, L. Niu, M. C. Liu, L. Lin, T. Chen, Y. Gong, C. Li, X. Liu, S. Xu, *ChemSusChem* **2019**, *12*, 3571–3581.
[69] J. Wang, D. Zhang, F. Nie, R. Zhang, X. Fang, Y. Wang, *Environ. Sci. Pollut. Res. Int.* **2023**, *30*, 15377–15391.
[70] M. C. Biesinger, *Appl. Surf. Sci.* **2022**, *597*, e153681.
[71] C. Zhu, X. Dong, X. Mei, M. Gao, K. Wang, D. Zhao, *J. Mater. Sci.* **2020**, *55*, 17108–17119.
[72] Z. Li, J. Wang, X. Liu, S. Liu, J. Ou, S. Yang, *J. Mater. Chem.* **2011**, *21*, 3397–3403.
[73] D. Wang, K. Wang, L. Sun, H. Wu, J. Wang, Y. Zhao, L. Yan, Y. Luo, K. Jiang, Q. Li, S. Fan, J. Li, J. Wang, *Carbon* **2018**, *139*, 145–155.
[74] R. Bardestani, G. S. Patience, S. Kaliaguine, *Can. J. Chem. Eng.* **2019**, *97*, 2781–2791.
[75] M. Thommes, K. Kaneko, A. V. Neimark, J. P. Olivier, F. Rodriguez-Reinoso, J. Rouquerol, K. S. W. Sing, *Pure Appl. Chem.* **2015**, *87*, 1051–1069.
[76] A. Noori, M. F. El-Kady, M. S. Rahmanifar, R. B. Kaner, M. F. Mousavi, *Chem. Soc. Rev.* **2019**, *48*, 1272–1341.
[77] N. Jabeen, A. Hussain, Q. Xia, S. Sun, J. Zhu, H. Xia, *Adv. Mater.* **2017**, *29*, e1700804.
[78] L. Athouël, F. Moser, R. Dugas, O. Crosnier, D. Bélanger, T. Brousse, *J. Phys. Chem. C* **2008**, *112*, 7270–7277.

[79] H. Jung, M. Taillefert, J. Sun, Q. Wang, O. J. Borkiewicz, P. Liu, L. Yang, S. Chen, H. Chen, Y. Tang, *J. Am. Chem. Soc.* **2020**, *142*, 2506–2513.

[80] J. Wang, J. Polleux, J. Lim, B. Dunn, *J. Phys. Chem. C* **2007**, *111*, 14925–14931.

[81] J. Zhao, A. F. Burke, *Adv. Energy Mater.* **2020**, *11*, e2002192.

[82] S. Paul, K. S. Choi, D. J. Lee, P. Sudhagar, Y. S. Kang, *Electrochim. Acta* **2012**, *78*, 649–655.

[83] A. S. Vedpathak, M. A. Desai, S. Bhagwat, S. D. Sartale, *Energy Fuels* **2022**, *36*, 4596–4608.

[84] A. R. C. Bredar, A. L. Chown, A. R. Burton, B. H. Farnum, *ACS Appl. Energ. Mater.* **2020**, *3*, 66–98.

[85] D. Qu, W. Ji, H. Qu, *Commun. Mater.* **2022**, *3*, e61.

[86] P. Scheitenberger, S. Brimaud, M. Lindén, *Mater Adv* **2021**, *2*, 3940–3953.

[87] A. Adán-Más, T. M. Silva, L. Guerlou-Demourgues, M. F. Montemor, *Electrochim. Acta* **2018**, *289*, 47–55.

[88] Q. A. Huang, Y. Li, K. C. Tsay, C. Sun, C. Yang, L. Zhang, J. Zhang, *J. Power Sources* **2018**, *400*, 69–86.

[89] B. Yan, M. Li, X. Li, Z. Bai, L. Dong, D. Li, *Electrochim. Acta* **2015**, *164*, 55–61.

[90] Z. Wei, Z. Zhang, Y. Ren, H. Zhao, *Front. Chem.* **2021**, *9*, e646218.

[91] X. Li, J. Liu, M. N. Banis, A. Lushington, R. Li, M. Cai, X. Sun, *Energy Environ. Sci.* **2014**, *7*, 768–778.

[92] L. Feng, Z. Xuan, H. Zhao, Y. Bai, J. Guo, C. W. Su, X. Chen, *Nanoscale Res. Lett.* **2014**, *9*, e290.

[93] E. Umeshbabu, M. Satyanarayana, G. Karkera, A. Pullamsetty, P. Justin, *Mater Adv* **2022**, *3*, 1642–1651.

[94] J. Kang, J. Wen, S. H. Jayaram, A. Yu, X. Wang, *Electrochim. Acta* **2014**, *115*, 587–598.

[95] D. Bresser, D. Buchholz, A. Moretti, A. Varzi, S. Passerini, *Energy Environ. Sci.* **2018**, *11*, 3096–3127.

[96] N. Böckenfeld, S. S. Jeong, M. Winter, S. Passerini, A. Balducci, *J. Power Sources* **2013**, *221*, 14–20.

[97] G. Greczynski, L. Hultman, *Prog. Mater. Sci.* **2020**, *107*, e100591.